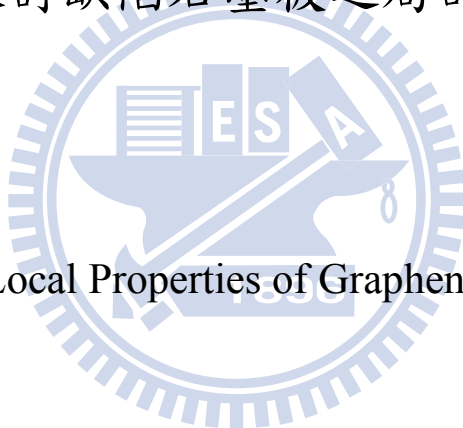# 國 立 交 通 大 學

機械工程學系

碩 士 論 文

探討缺陷石墨板之局部性質

Investigating Local Properties of Graphene Sheet with Defect

研 究 生 ：謝孟哲

指導教授 ：蔡佳霖 博士

中 華 民 國 九 十 九 年 七 月

探討缺陷石墨板之局部性質

Investigating Local Properties of Graphene Sheet with Defect

研 究 生：謝孟哲　　　　　　　　Student：Meng-Jhe Sie

指導教授：蔡佳霖　　　　　　　　Advisor：Jia-Lin Tsai

國 立 交 通 大 學

機 械 工 程 學 系

碩 士 論 文

A Thesis

Submitted to Department of Mechanical Engineering

College of Engineering National Chiao Tung University

in partial Fulfillment of the Requirements

for the Degree of Master

in

Mechanical Engineering

July 2010

Hsinchu, Taiwan, Republic of China

中 華 民 國 九 十 九 年 七 月

探討缺陷石墨板之局部性質

學生：謝孟哲　　　　　　　　　　指導教授：蔡佳霖

國立交通大學機械工程學系碩士班

摘　要

　　本研究目的在探討具有自由面和裂紋之石墨板受到單軸拉伸載重下之局部性質。利用分子動力模擬，可以得到石墨板受到單軸拉伸外力下，各個碳原子的平衡位置。接著利用 Hardy，Lutsko 以及 Tsai 所提出的局部應力公式，可以計算出石墨板之局部應力場。對於具有自由面的石墨板，研究結果顯示在無應力(stress free)的條件下且凡德瓦爾(van der Waals)力存在時，石墨板之自由面存在著壓縮應力，其他部分則受到些微的拉伸應力;而在無應力(stress free)且凡德瓦爾力不存在的條件下，石墨板的每個位置均沒有受力。

　　對於具有裂紋之石墨板，同樣先利用分子動力模擬得到拉伸載重下碳原子的平衡位置。接著利用局部應力公式以及線彈性破壞力學(linear elastic fracture mechanics)，有限元素法(finite element method)和非局部彈性理論(non-local elasticity theory)來探討裂紋端附近的應力場。研究結果顯示，線

彈性破壞力學以及有限元素法的裂紋應力場皆顯示出應力奇異性(stress singularity)，且在小裂紋情況下，線彈性破壞力學與有限元素法的應力場有明顯的差異；而 Hardy 的應力場在靠近裂紋附近顯示出非局部(non-local)性質，所得到的最大應力與非局部理論解非常近似。另外由 Hardy 的應力場，也能直接從最大應力推導出石墨板之破壞性質。分析結果顯示，由 Hardy 應力場所得到的應力強度因子(stress intensity factor)與有限元素和線彈性破壞力學一致；而破裂韌性(fracture toughness)在裂紋長度小於 40 個晶格時，會隨著裂紋長度變小而降低；在裂紋長度大於 40 個晶格的時候，破裂韌性才會趨於一個常數定值，此結果與非局部理論所推導出的結果一致。因此，應力強度因子可有效地描述裂紋附近的應力場，而破裂韌性並不適合用來描述具有小裂紋的破壞性質。

Investigating Local Properties of Graphene Sheet with Defect

Student：Meng-Jhe Sie   Advisor：Dr. Jia-Lin Tsai

Department of Mechanical Engineering

National Chiao Tung University

Abstract

This paper aims to investigate the local properties of graphene sheet with free surface or central cracks subjected to uniaxial loading. The equilibrium configuration of the graphene sheet subjected to uniaxial loading was determined through molecular dynamic (MD) simulation. For the graphene with free surfaces, three local stress formulations, i.e., Hardy, Lutsko and Tsai stress, were employed to calculate the local stress distribution near the free surfaces. It was found that when van der Waals force was present, only Hardy stress expression can describe the stress field effectively. Results indicated that the graphene sustained compressive stress on the edge and tensile stress in the interior at stress free state. On the other hand, when van der Waals force was absent, both Hardy and Tsai stress can describe the stress distribution accurately. Results showed that the graphene sustained zero stress at every position at stress free state such that the bond length did not alter.

Regarding the graphene with central cracks subjected to remote tensile loading, both the atomistic and continuum stress were employed to investigate the local stress distribution near the crack tip. For the discrete graphene sheet, Hardy and Tsai stress were adopted to calculate the near-tip stress field of the graphene in the absence of van der Waals interaction. For the continuum models, finite element method was used to calculate the stress

distribution. In order to describe the numerical results, two analytical solutions were incorporated, such as linear elastic fracture mechanics (LEFM) and the non-local elasticity solution. Results showed that for both LEFM and FEM solutions, the stress fields demonstrated the $1/\sqrt{x}$ stress singularity near the crack tip. In addition, it was found LEFM solution cannot describe the stress accurately when the crack length is small. On the other hand, atomistic stress such as Hardy and Tsai stress yielded a more reasonable finite stress near the tip. It was found that the maximum stress obtained from Hardy's formulation was in agreement with the non-local elasticity solution, whereas Tsai's maximum stress is larger than the analytical solution; therefore only Hardy stress field exhibited non-local attribute near the crack tip. Based on the maximum stress hypotheses, the fracture properties such as stress intensity factor and fracture toughness were deduced directly from local stress field. Results indicated that stress intensity factor derived from Hardy stress field was in agreement with the FEM and the actual solution of LEFM. On the other hand, the fracture toughness defined in LEFM is found to be cracksize dependent when the crack length is small for discrete models. For crack lengths below 40 lattices, the fracture toughness would decrease with the decrease of the crack lengths; the result was in agreement with the non-local elasticity solution. Therefore, the fracture toughness defined as a material property may not be suitable for describing fracture with small cracks.

Table of Content

LIST OF TABLES

LIST OF FIGURES

Chapter 1 Introduction

1.1 Research Motive

Graphene sheet, because of their superior mechanical performances and light weight properties, have been extensively employed in nanocomposites. This study aims to investigate the local properties of graphene sheet with free surface or central cracks. It is well known that the nanostructure of the graphene sheet may influence the mechanical performance of the nanocomposites. However, few studies have studied the local properties of the graphene sheet which are very crucial to composite design and application. In this paper, the local stress formulations, i.e. Hardy stress, Tsai stress and Lutsko stress, as well as the analytical solutions are introduced to investigate the local properties of the graphene sheet. Based on the local stress distributions, the influence of the nanostructure was characterized.

1.2 Paper Review

With the development of nanotechnology, the characterization of the mechanical properties in nano-scale is becoming an essential task and attracting lots of attention in materials community. The atomistic simulations with the advantage of simplicity have been employed to understand the fundamental mechanical properties of nanomaterials. For the nanomaterials with discreet characteristic, the stress originated based on the continuum concept would become an ambiguous physical quantity in atomistic scale. However, the determination of stress is necessary in atomistic simulation in order to correctly evaluate the mechanical properties of the materials. By considering the momentum change and the interatomistic interaction, several stress definitions suitable for the atomistic simulation have been developed. Virial

stress [1] derived from the virial theorem is first proposed and has been widely used in molecular dynamic (MD) simulations. Nevertheless, for the materials with defects or inhomogeneous deformation, only the averaged response can be demonstrated by the virial stress, and thus the "local" information which is essential in the defected material can not be clearly presented [2]. In order to modify the forward-mentioned problems, other stresses, such as Tsai stress [3], Lutsko stress [4], BDT stress [5] and Hardy stress [6] were proposed and implemented in the molecular simulation. Sun et al. [7] has systematically compared virial stress and Tsai stress and indicated that they are mathematically equivalent in calculating the overall average stress, whereas in calculating local stress distribution, virial stress exhibits unreasonable result, i.e. nonzero normal stress at free surface. As a result, Tsai's formula is more accurate than virial stress in describing the local stress field. Zimmerman and Web et al. [8, 9] based on their numerical simulations, demonstrated that Hardy stress is appropriate for both homogeneous and inhomogeneous deformation. For systems subjected to deformation, finite temperature, or both, the Hardy description of stress displays an accurate value expected from continuum theory; for the system with free surface, Hardy's expression near the surface is found to be consistent with the mechanical definition of stress. Moreover, it is very accurate and robust, and superior to BDT and Lutsko stress formulation in the local stress calculation. However, few studies concerning the local stress field of the graphene sheet with free surfaces have been reported.

One of the crucial defects in the graphene sheet is the crack, which was created during the manufacturing process. Hashimoto et al. [10] has observed several atomic defects in graphene layers by transmission electron microscopy (TEM). Meyer et al. [11] also observed some point defects in the graphene sheet by transmission electron microscopy (TEM). It seems that cracks are a common defect existing in the graphene sheet; however, few studies have examined the local properties of the cracked

graphene, especially from the stress point of view. Tsai et al. [12] has adopted Hardy

stress expression to investigate the local stress field of the graphene sheet with central

cracks. In their study, they indicated that the stress intensity factor defined based on

singular assumption may not be suitable for describing the fracture in the discrete

model. Jin and Yuan [13] utilized virial stress formula to investigate the local stress

field near the crack tip of the central-cracked graphene subjected to remote uniaxial

loading. However, in their study, they did not discuss the local properties

comprehensively. In addition, they did not demonstrate the applicability of virial

stress in describing the near-tip stress field, since it is found that virial stress is

inappropriate for calculating the local stress distribution [2, 7].

1.3 Research Approach

The outline of the thesis and the primary tasks of each chapter are addressed as

the following. The graphene sheet with free surfaces or central cracks subjected to

uniaxial loading was constructed through molecular dynamic simulation. The detail of

the simulation procedures and associated potential functions and force fields were

illustrated in Chapter 2.

For the graphene sheet with free surfaces, three local stress formulations, i.e.,

Hardy stress, Lutsko stress, and Tsai stress were introduced to investigate the local

stress distribution. Graphene sheet with and without long-range interaction, i.e. van

der Waals force, was discussed, respectively. In order to demonstrate the applicability

of local stress formulations, a periodic single-layer graphene sheet under uniaxial

loading was constructed and discussed in advance, from which the accuracy of the

formulations can be verified. After the determination of local stress formulations, the

local stress distribution of the graphene with free surfaces under uniaxial loading was

investigated and the results were presented in Chapter 3.

In addition to the free surface, graphene sheet with central cracks subjected to remote uniaxial loading is another concern. Discrete graphene models with different central crack lengths were constructed, respectively, in which Hardy and Tsai stress expressions were employed to investigate the local stress distribution near the crack tip. For the comparing purpose, the continuum graphene models with the same geometry and line cracks were also constructed by finite element method, and the corresponding near-tip stress field was compared and discussed in detail. In order to examine the above local stress fields, two analytical solutions, i.e. linear elastic fracture mechanics and non-local elasticity solutions were incorporated. Based on the numerical and analytical results of local stress calculations, the fracture properties of the cracked graphene subjected to remote uniaxial loading can be deduced. The discussion was presented in Chapter 4.

Finally, the conclusions of the thesis were summarized in the Chapter 5.
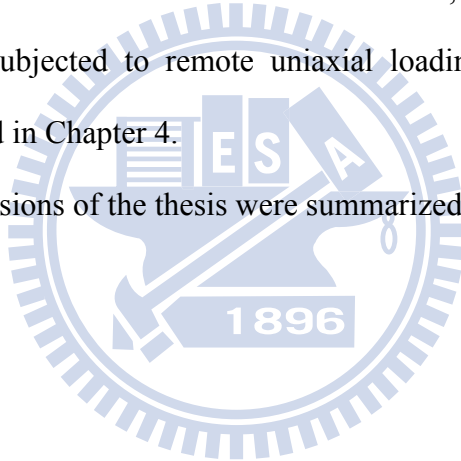
Chapter 2 Molecular dynamic simulation

The atomistic structure of graphene sheet subjected to uniaxial loading was constructed through molecular dynamic simulations. In this chapter, the potential functions for describing the interaction between carbon atoms of graphene were presented. Two kinds of potential functions are introduced, i.e. intermolecular function and intramolecular function. Subsequently, the molecular dynamic simulation procedures were presented. The modified NPT ensemble was employed to construct the graphene sheet subjected to uniaxial loading. With the potentials and simulation procedures described, the atomistic structure of the graphene sheet subjected to uniaxial loading can be constructed accordingly.

2.1 Construction of atomistic structure of graphene sheet

Graphene is constructed by carbon atoms arranged in hexagonal pattern. The interatomistic distance between the adjacent carbon atoms is 1.42 Å, and the associated atomistic interaction is covalently bonded by SP^2 hybridized electrons, the bond angle of which is 120° to each other [14]. In order to investigate the local stress field of the graphene, the atomistic structures have to be constructed in advance together with the appropriately specified atomistic interaction. In describing the graphene, two kinds of atomistic interactions are normally taken in account: one is bonded interaction, such as the covalent bond, and the other is the non-bonded interaction, i.e., van der Waals and electrostatic forces. Among the atomistic interactions, the covalent bond between two neighboring carbon atoms that provides the building block of the primary structure of the graphite may play an essential role in the mechanical responses. Such bonded interaction can be described using the potential energy that consists of bond stretching, bond angle bending, torsion, and inversion [15]. As a result, the total potential energy of the graphite contributed from

the covalent bond can be written explicitly as

$$U_{total} = U_{stretch} + U_{angle} + U_{dihedral} + U_{inversion} + U_{vdW} \qquad (2.1.1)$$

where $U_{stretch}$ is a bond stretching potential, U_{angle} is a bond angle bending potential, $U_{dihedral}$ is a dihedral angle torsional potential, and $U_{inversion}$ is an inversion potential. For graphite structures under in-plane deformation, the atomistic interaction is mainly governed by the bond stretching and bond angle bending; therefore, the dihedral torsion and inversion potentials that are related to the out-of-plane deformation can be disregarded in the modeling. The explicit form for the bond stretching and bond angle bending can be approximated in terms of elastic springs as [16]

$$U_{stretch}(r_{ij}) = \frac{1}{2} k_r (r_{ij} - r_0)^2 \qquad (2.1.2)$$

$$U_{angle}(\theta_{jik}) = \frac{1}{2} k_\theta (\theta_{jik} - \theta_0)^2 \qquad (2.1.3)$$

where k_r and k_h are the bond stretching force constant and angle bending force constant, respectively. The constants k_r=938 kcal/mol-Å^2，k_θ=126 kcal/mol-rad^2 selected from AMBER force field for carbon–carbon atomic-interaction [17] are employed in the molecular simulation. The parameters r_0 and θ_0 represent bond length and bond angle in equilibrium position, which are assumed to be 1.42 Å and 120°, respectively, for the graphite atomistic structures. In addition to the bonded interaction, the non-bonded interaction between the carbon atoms is regarded as the van der Waals force, which can be characterized using the equivalent Lennard-Jones (L-J) potential as

$$U_{vdW}(r_{ij}) = \left(\frac{A}{r_{ij}^{12}}\right) - \left(\frac{B}{r_{ij}^{6}}\right) \qquad (2.1.4)$$

where r_{ij} is the distance between the non-bonded pair of atoms. For the hexagonal graphite, the parameters A $=530739.960$ Å^{12}Kcal/mole, B $=343.564502$Å^{6}Kcal/mole suggested in the literature [16] were adopted in the modeling. Moreover, the cutoff distance for the van der Waals force is assigned to be 10 Å, which means that beyond this distance, van der Waals interactions are small enough to be ignored. In atomistic mechanics, all atoms except those that are bound to each other or connected to a common atom have to be accounted for in the calculation of van der Waals interactions [18].

The atomistic structures of graphene sheet with a stress-free state was obtained by performing the modified NPT ensemble with the characteristics of varying simulation box in shape and size [19] in the MD simulation at the time increment of 1 fs for 100 ps. Subsequently, the uniaxial tensile stress was applied on the graphene sheet in the y direction. After the modified NPT ensemble with time increment at 1 fs for 100 ps was performed, the deformed atomistic configuration of graphene sheet under the applied loading was obtained. It is noted that in the study, the DL-POLY package originally developed by Daresbury Laboratory [20] was modified to simulate the uniaxial loading on the graphene sheet.

2.2 Amber force field

In calculating the local stress field, one must obtain the interaction force between the atoms. Followed by the DL_POLY user manual [20], the force field derived from the above potential was presented in this section. There are three kinds of interaction force in this study.

(1) Stretching bond

The stretching bond potential between atom i and atom j is expressed as

$$U(r_{ij}) = \frac{1}{2}k_r(r_{ij} - r_0)^2. \tag{2.2.1}$$

Therefore the interaction force can be obtained as

$$\mathbf{f}_h = -\frac{\partial U(r_{ij})}{\partial \mathbf{r}_h} = -\frac{\partial U(r_{ij})}{\partial r_{ij}}\frac{\partial r_{ij}}{\partial \mathbf{r}_h}, \tag{2.2.2}$$

where h can be atom i or atom j. The first and second term in the RHS of eqn. (2.2.2) can be expressed, respectively as

$$\frac{\partial U(r_{ij})}{\partial r_{ij}} = \frac{\partial}{\partial r_{ij}}\left[\frac{1}{2}k_r(r_{ij} - r_0)^2\right] = k_r(r_{ij} - r_0) \tag{2.2.3}$$

$$\frac{\partial r_{ij}}{\partial \mathbf{r}_h} = \frac{\partial}{\partial \mathbf{r}_h}\left[(\mathbf{r}_j - \mathbf{r}_i)\cdot(\mathbf{r}_j - \mathbf{r}_i)\right]^{1/2} = \frac{1}{2}\left(\frac{1}{r_{ij}}\right)\frac{\partial}{\partial \mathbf{r}_h}(\mathbf{r}_j^2 - 2\mathbf{r}_j\mathbf{r}_i + \mathbf{r}_i^2) \tag{2.2.4}$$

with

$$\frac{\partial}{\partial \mathbf{r}_h}(\mathbf{r}_j^2 - 2\mathbf{r}_j\mathbf{r}_i + \mathbf{r}_i^2) = (2\mathbf{r}_j\delta_{jh} - 2\delta_{jh}\mathbf{r}_i - 2\delta_{ih}\mathbf{r}_j + 2\mathbf{r}_i\delta_{ih}) = 2(\delta_{jh}\mathbf{r}_{ij} - \delta_{ih}\mathbf{r}_{ij}) \tag{2.2.5}$$

As a result, the force field of stretching bond can be obtained as

$$\mathbf{f}_h = \frac{-k_r(r_{ij} - r_0)}{r_{ij}}(\delta_{jh}\mathbf{r}_{ij} - \delta_{ih}\mathbf{r}_{ij}) \tag{2.2.6}$$

(2) Angle bending bond

The angle bending bond potential between atom i, atom j and atom k is expressed as

$$U(\theta_{jik}) = \frac{1}{2}k_\theta(\theta_{jik} - \theta_0)^2. \tag{2.2.7}$$

Therefore the force exerting on atom h is

$$\mathbf{f}_h = -\frac{\partial U(\theta_{jik})}{\partial \mathbf{r}_h} = -\frac{\partial U(\theta_{jik})}{\partial \theta_{jik}} \frac{\partial}{\partial \mathbf{r}_h}\left\{\cos^{-1}\left(\frac{\mathbf{r}_{ij} \cdot \mathbf{r}_{ik}}{r_{ij}r_{ik}}\right)\right\}, \tag{2.2.8}$$

where h can be atom i, atom j, or atom k. The first and second term in the RHS of eqn. (2.2.8) can be expressed, respectively as

$$-\frac{\partial U(\theta_{jik})}{\partial \theta_{jik}} = -\frac{\partial}{\partial \theta_{jik}}\left[\frac{1}{2}k_\theta(\theta_{jik} - \theta_0)^2\right] = -k_\theta(\theta_{jik} - \theta_0) \tag{2.2.9}$$

$$\frac{\partial}{\partial \mathbf{r}_h}\left\{\cos^{-1}\left(\frac{\mathbf{r}_{ij} \cdot \mathbf{r}_{ik}}{r_{ij}r_{ik}}\right)\right\} = \frac{\partial}{\partial \mathbf{r}_h}\left\{\cos^{-1}x\right\} = \frac{\partial \cos^{-1}x}{\partial x}\frac{\partial x}{\partial \mathbf{r}_h}, \tag{2.2.10}$$

where x=cosθ. The first and second term in the RHS of eqn. (2.2.10) can be expressed as

$$\frac{\partial \cos^{-1}x}{\partial x} = -\frac{1}{\sqrt{1-x^2}} = -\frac{1}{\sin \theta} \tag{2.2.11}$$

$$\frac{\partial x}{\partial \mathbf{r}_h} = \frac{\mathbf{r}_{ik}}{r_{ij}r_{ik}}\frac{\partial}{\partial \mathbf{r}_h}(\mathbf{r}_{ij}) + \frac{\mathbf{r}_{ij}}{r_{ij}r_{ik}}\frac{\partial}{\partial \mathbf{r}_h}(\mathbf{r}_{ik}) + \mathbf{r}_{ij} \cdot \mathbf{r}_{ik}\frac{\partial}{\partial \mathbf{r}_h}\left\{\frac{1}{r_{ij}r_{ik}}\right\}. \tag{2.2.12}$$

Introducing eqn. (2.2.11) and (2.2.12) into eqn. (2.2.10), one can obtain the force field of angle bending bond as

$$\mathbf{f}_h = \frac{-k_\theta(\theta_{jik} - \theta_0)}{\sin(\theta_{jik})}$$
$$\left\{(\delta_{hj} - \delta_{hi})\frac{\mathbf{r}_{ik}}{r_{ij}r_{ik}} + (\delta_{hk} - \delta_{hi})\frac{\mathbf{r}_{ij}}{r_{ij}r_{ik}} - \cos(\theta_{jik})\left[(\delta_{hj} - \delta_{hi})\frac{\mathbf{r}_{ij}}{r_{ij}^2} + (\delta_{hk} - \delta_{hi})\frac{\mathbf{r}_{ik}}{r_{ik}^2}\right]\right\}.$$

$$\tag{2.2.13}$$

(3) van der Waals force

The van der Waals potential between atom i and atom j is expressed as

$$U(r_{ij}) = \left(\frac{A}{r_{ij}^{12}}\right) - \left(\frac{B}{r_{ij}^{6}}\right).$$

(2.2.14)

Therefore the interaction force can be obtained as

$$\mathbf{f}_h = -\frac{\partial U(r_{ij})}{\partial \mathbf{r}_h} = -\frac{\partial U(r_{ij})}{\partial r_{ij}} \frac{\partial r_{ij}}{\partial \mathbf{r}_h},$$

(2.2.15)

where h can be atom i or atom j. The first term in the RHS of eqn. (2.2.15) can be expressed as

$$\frac{\partial U(r_{ij})}{\partial r_{ij}} = \frac{\partial}{\partial r_{ij}}\left(\frac{A}{r_{ij}^{12}} - \frac{B}{r_{ij}^{6}}\right) = -\left(12\frac{A}{r_{ij}^{13}} - 6\frac{B}{r_{ij}^{7}}\right).$$

(2.2.16)

The second term in the RHS of eqn. (2.2.15) is identical to eqn. (2.2.4). As a result, the force field of van der Waal can be obtained as

$$\mathbf{f}_h = \left(12\frac{A}{r_{ij}^{13}} - 6\frac{B}{r_{ij}^{7}}\right)\frac{(\delta_{jh}\mathbf{r}_{ij} - \delta_{ih}\mathbf{r}_{ij})}{r_{ij}}.$$

(2.2.17)

With the force fields described above, one can employ them into the calculation of local stress.

Chapter 3 Local stress distribution of graphene with free surfaces

In this chapter, Hardy stress along with other stress formulations, such as Tsai stress and Lutsko stress were employed to calculate the local stress distribution of graphene sheet with free surfaces. The purpose of the study is to investigate the stress distribution in the vicinity of free surface such that the applicability of local stress formulations can be demonstrated when free surfaces are present. Furthermore, the effect of free surface on the morphology of the graphene sheet associated with stress distribution was discussed.

3.1 Local stress formulations

Tsai's expression of local stress [3] is inherently the macroscopic description of stress-- the intermolecular force acting on the plane-- and at zero temperature it is expressed as

$$\vec{t} = \frac{1}{\delta A} \sum_{\alpha\beta \cap \delta A} \vec{f}_{\alpha\beta},$$

(3.1.1)

where δA denotes the area of the dividing plane and $f^{\alpha\beta}$ is the interatomistic force between atom α and β acting on the plane. For the graphene system, the dimension of the dividing plane adopted in the study, shown in Fig. 3.1.1, is 3.4×2.46 Å corresponding to the thickness and lattice length of the graphene. Another local stress formulation was proposed by Lutsko [21] and extended by Cormier et al. [4]. At zero temperature, it is expressed as

$$\sigma_{ij}{}^{avg} = \frac{1}{2\Omega} \sum_{\alpha=1}^{N} \sum_{\beta \neq \alpha}^{N} r_i{}^{\alpha\beta} F_j{}^{\alpha\beta} l^{\alpha\beta},$$

(3.1.2)

where Ω is the averaging volume, $r^{\alpha\beta}$ and $F^{\alpha\beta}$ represent the distance and force between atom α and β, respectively. Moreover, $l^{\alpha\beta}$ denotes the fraction of the length of the $\alpha-\beta$ bond lying inside the averaging volume and its value is $0 \leq l^{\alpha\beta} \leq 1$. The averaging volume employed in the graphene is a sphere with radius of 3.4 Å. In this paper, Hardy stress formulation is the main concern and will be compared with the above formulations; therefore, in the following subsection, the Hardy formulation is briefly reviewed.

Hardy derived the stress formulation based on the three assumptions, in which the mass density, momentum density and energy density are expressed as

$$\rho(\mathbf{r},t) = \sum_{\alpha=1}^{N} m^{\alpha} \psi(\mathbf{r}^{\alpha} - \mathbf{r}) \tag{3.1.3}$$

$$\mathbf{p}(\mathbf{r},t) = \sum_{\alpha=1}^{N} m^{\alpha} \mathbf{v}^{\alpha} \psi(\mathbf{r}^{\alpha} - \mathbf{r}) \tag{3.1.4}$$

$$E^{0}(\mathbf{r},t) = \sum_{\alpha=1}^{N} \left\{ \frac{1}{2} m^{\alpha} (\mathbf{v}^{\alpha})^{2} + \phi^{\alpha} \right\} \psi(\mathbf{r}^{\alpha} - \mathbf{r}) \tag{3.1.5}$$

where ρ, p and E^0 represent the mass density, linear momentum and energy density, respectively; m^{α}, v^{α}, r^{α} and ϕ^{α} represent the mass, velocity, position and potential energy of atom α, respectively. The localization function ψ serves the purpose of spreading out the properties of atoms to the space r, allowing each atom to contribute to the continuum properties. From the above equations and introducing the conservation of linear momentum, Hardy derived the local stress field in the following manner.

1. Taking the derivative of eq. (3.1.3) with respect to time

$$\frac{\partial \mathbf{p}}{\partial t} = \frac{\partial}{\partial t}\left(\sum_{\alpha=1}^{N} m^{\alpha} \mathbf{v}^{\alpha} \psi(\mathbf{r}^{\alpha} - \mathbf{r})\right) = \sum_{\alpha=1}^{N}\left[\mathbf{F}^{\alpha} \psi(\mathbf{r}^{\alpha} - \mathbf{r}) + m^{\alpha} \mathbf{v}^{\alpha}(-\mathbf{v}^{\alpha}\frac{\partial \psi(\mathbf{r}^{\alpha} - \mathbf{r})}{\partial \mathbf{r}})\right],$$

$$(3.1.6)$$

where F^{α} is the force acting on atom α. According to an assumption made by Hardy, the force on any atom α can be written as

$$\sum_{\alpha=1}^{N}\mathbf{F}^{\alpha}\psi(\mathbf{r}^{\alpha} - \mathbf{r}) = \sum_{\alpha=1}^{N}\sum_{\beta\neq\alpha}^{N}\mathbf{F}^{\alpha\beta}\psi(\mathbf{r}^{\alpha} - \mathbf{r}). \qquad (3.1.7)$$

Since the potential employed in the present study is in the pair-wise form, $F^{\alpha\beta}$ represents the force exerted on atom α from atom β. Moreover, based on Newton's third law, $F^{\alpha\beta} = - F^{\alpha\beta}$, the above equation can be rewritten as the following

$$\sum_{\alpha=1}^{N}\mathbf{F}^{\alpha}\psi(\mathbf{r}^{\alpha} - \mathbf{r}) = \frac{1}{2}\sum_{\alpha=1}^{N}\sum_{\beta\neq\alpha}^{N}\mathbf{F}^{\alpha\beta}\left[\psi(\mathbf{r}^{\alpha} - \mathbf{r}) - \psi(\mathbf{r}^{\beta} - \mathbf{r})\right] \qquad (3.1.8)$$

2. For the purpose of making the stress expression simple and plain, Hardy defined the bond function $B^{\alpha\beta}$ as

$$B^{\alpha\beta}(\mathbf{r}) \equiv \int_{0}^{1} \psi(\lambda\mathbf{r}^{\alpha\beta} + \mathbf{r}^{\beta} - \mathbf{r})d\lambda, \qquad (3.1.9)$$

where $r^{\alpha\beta} = r^{\alpha} - r^{\beta}$. In order to obtain some insight into the bond function, the integration can be written in the summation form

$$B^{\alpha\beta}(\mathbf{r}) \equiv \sum_{n=1}^{m} \psi(\mathbf{r}^n)\Delta\lambda = \left[\psi(\mathbf{r}^1) + ... + \psi(\mathbf{r}^m)\right]\frac{1}{m}, \qquad (3.1.10)$$

where r^1 and r^m represent r^β-r and r^α-r, respectively, as illustrated in Fig. 3.1.2. From eq. (3.1.10) and Fig. 3.1.2, it is clear to see that the bond function spreads out the property of bond by dividing the length between atom α and β into several segments and allowing each segment to contribute to the space x. By taking the derivative of ψ in eq. (3.1.9) with respect to λ

$$\frac{\partial\psi(\lambda\mathbf{r}^{\alpha\beta} + \mathbf{r}^\beta - \mathbf{r})}{\partial\lambda} = -\frac{\partial\psi(\lambda\mathbf{r}^{\alpha\beta} + \mathbf{r}^\beta - \mathbf{r})}{\partial\mathbf{r}}\mathbf{r}^{\alpha\beta}, \qquad (3.1.11)$$

and integrating both sides of the above equation with respect to λ from 0 to 1, respectively, the following relation can be obtained

$$\psi(\mathbf{r}^\alpha - \mathbf{r}) - \psi(\mathbf{r}^\beta - \mathbf{r}) = -\mathbf{r}^{\alpha\beta}\frac{\partial B^{\alpha\beta}(\mathbf{r})}{\partial\mathbf{r}}. \qquad (3.1.12)$$

Therefore, along with eq. (3.1.7) to eq. (3.1.12), the time derivative of linear momentum density can be written as

$$\frac{\partial\mathbf{p}}{\partial t} = -\frac{\partial}{\partial\mathbf{r}}\left\{\sum_{\alpha=1}^{N}\left[m^\alpha\mathbf{v}^\alpha \otimes \mathbf{v}^\alpha\psi(\mathbf{r}^\alpha - \mathbf{r})\right] + \frac{1}{2}\sum_{\alpha=1}^{N}\sum_{\beta\neq\alpha}^{N}\mathbf{r}^{\alpha\beta} \otimes \mathbf{F}^{\alpha\beta}B^{\alpha\beta}(\mathbf{r})\right\}. \qquad (3.1.13)$$

3. From the continuum balance of linear momentum, the following relation can be obtained

$$\frac{\partial \mathbf{p}}{\partial t} = \frac{\partial}{\partial \mathbf{x}}\left(\boldsymbol{\sigma} - \rho \mathbf{v} \otimes \mathbf{v}\right), \tag{3.1.14}$$

where σ, ρ, v denotes continuum stress, mass density and velocity, respectively. Hence eq. (3.1.13) and (3.1.14) can be connected and expressed as

$$\boldsymbol{\sigma}(\mathbf{r}) = -\left\{\sum_{\alpha=1}^{N} m^{\alpha}\left(\mathbf{v}^{\alpha} - \mathbf{v}\right) \otimes \left(\mathbf{v}^{\alpha} - \mathbf{v}\right)\psi(\mathbf{r}^{\alpha} - \mathbf{r}) + \frac{1}{2}\sum_{\alpha=1}^{N}\sum_{\beta \neq \alpha}^{N} \mathbf{r}^{\alpha\beta} \otimes \mathbf{F}^{\alpha\beta} B^{\alpha\beta}(\mathbf{r})\right\} \tag{3.1.15}$$

where m^{α}, v^{α}, r^{α} represent the mass, velocity and position of atom α, respectively; v and ψ represent the continuum velocity and localization function, respectively. It is noted that when the system is simulated at 0 K, the kinetic contribution of eq. (3.1.15) is zero. As a result, Hardy's local stress field can be finally derived as

$$\sigma_{ij}(\mathbf{r},t) = -\left(\frac{1}{2}\sum_{\alpha=1}^{N}\sum_{\beta \neq \alpha}^{N} r_i^{\alpha\beta} F_j^{\alpha\beta} B^{\alpha\beta}(\mathbf{r})\right). \tag{3.1.16}$$

From Hardy's stress expression, one can see that the localization function plays an important role in the calculation of stress. In this study, Gaussian function with normal distribution property is employed in Hardy's formula. As a result, ψ is expressed as

$$\psi(\mathbf{r}^{\alpha} - \mathbf{r}, h) = \frac{1}{(\sqrt{\pi}h)^d}\exp\left(-\frac{(\mathbf{r}^{\alpha} - \mathbf{r})^2}{h^2}\right), \tag{3.1.17}$$

where d is the dimension of the system and h is the smoothing length. Since the

graphene sheet can be viewed as a two-dimensional system with thickness of 3.4 Å [22], d is equal to 2 in this study. The smoothing length represents the way that the properties of discrete atoms are distributed to the continuum space. Different localization functions with various smoothing lengths are shown in Fig. 3.1.3. As one can see in the figure, a short smoothing length, such as h=1.8, represents a sharp drop in distribution while a long one stands for a smoothly-decayed distribution, like h equal to 3.0. It is noted that for 2-D Gaussian function, the following relation must be satisfied,

$$\iint_{R^2} \psi(\mathbf{x}) d^2 \mathbf{x} = 1. \tag{3.1.18}$$

Since the value of the function is approaching zero at long distances as shown in Fig. 3.1.3, for the purpose of reducing computing cost, an appropriate cut-off radius is needed in calculation. Table 3.1.1 lists the cut-off radius corresponding to each localization function with different smoothing lengths. With the cut-off radius suggested in Table 3.1.1, one can obtain a precise value with numerical error below 10^{-7} %. In this chapter, the smoothing length employed in Hardy's formulation is 2.5 and the corresponding cut-off radius is 9 Å.

3.2 The determination of local stress employed in graphene system

Before applying local stress formulations to the graphene sheet with free surface, a perfect graphene sheet with periodic boundary conditions imposed in the in-plane directions was constructed through molecular dynamic simulation, such that the accuracy of local stress formulations can be verified in advance. In addition, for the purpose of showing the applicability of local stress formulations in terms of atomistic interactions, two types of force fields are considered: one includes only bonded

interaction, such as covalent bond, and the other comprises bonded as well as non-bonded interactions, i.e. covalent bond and van der Waals. Followed by the procedures mentioned in the previous chapter, the atomistic structures of graphene sheet with a uniaxial stress state of 10 GPa was obtained by performing the modified NPT ensemble and then taken as an illustration as shown in Fig. 3.2.1. Fig. 3.2.2 shows the stress distribution of graphene sheet with only bonded interaction, i.e. covalent bond force field. From the figure, one can see that both Hardy and Tsai's local stress expressions demonstrate satisfactory accuracy of local stress distribution whereas a slight overestimate is found in Lutsko's stress expression. Fig. 3.2.3 shows the stress distribution of graphene sheet with bonded as well as non-bonded interactions, calculated by Hardy and Lutsko's formulations. It is apparent that Lutsko stress fluctuates substantially along the x axis while Hardy stress remains a uniform and precise distribution. For Tsai's stress formula, it is seen from Fig. 3.2.4 that with the increase of the width of dividing plane, the stress tends to converge to the external applied stress, i.e. 10 GPa. It is found, however, the stress converges to 10 GPa only until the width of the dividing plane is exactly the same as the simulation box, and hence the local stress distribution can not be exhibited. Therefore, based on the above discussion, it is known that for the graphene sheet with only bonded interaction, Hardy as well as Tsai's formulations are demonstrated to be appropriate for calculation of local stress; on the other hand, for the graphene sheet with bonded interactions as well as the non-bonded interaction, due to the presence of long-range interaction from van der Waals force, only Hardy stress formulation is suitable for calculating local stress. The graphene sheet with free surface in the x direction is shown in Fig. 3.2.5 and the position for stress calculation is the x axis.

3.3 Stress distribution in the graphene with covalent bond interaction

Similar to the procedures mentioned in the pervious chapter, the associated atomistic structures of graphene sheet with free surfaces with bonded interactions at the stress free state and uniaxial stress state of 10 GPa were obtained by performing the modified NPT ensemble. When the deformed configuration of the atomistic graphene structure is derived from the modified NPT ensemble, the corresponding local stress distribution can be calculated using Hardy, Lutsko and Tsai's stress formulations. As shown in Fig. 3.3.1, all three formulations result in a uniform zero stress at stress free state. The dotted lines marked in the figure locate the positions of the free surfaces. The corresponding morphology is shown in Fig. 3.3.2. It is apparent that with only the bonded potentials, the graphene sheet is quite stable at stress free state and hence the configuration does not alter. The stress distribution at uniaxial stress state (10 GPa) is shown in Fig. 3.3.3. It is noted that due to the difference of cross section areas between graphene sheet and simulation box, the actual load carried by the graphene is 14.4 GPa. As one can see from the figure, near the free surface, the local stress calculated from the three expressions begins to drop gradually due to the influence of free surface. The extent of the influence range from the free surface is dependent on the expression of the local stress formula. For Hardy and Lutsko stress, due to their larger radius employed in stress calculation (9Å and 3.4Å respectively), the stress drops at the position relatively far away from the surface; on the contrast, Tsai stress with smaller width of area (2.46 Å) begins to drop only at the surface. If a larger width of area (7.38 Å) is adopted in Tsai's formulation, the stress will drop at the position farther from the surface, as shown in Fig. 3.3.4. Besides, similar variation can be found in the morphology of graphene sheet, as shown in Fig. 3.3.5. Fig. 3.3.5 illustrates the elongation of bond length in the y direction along the x axis. Due to the applied uniaxial loading, the distance between atoms in y direction is elongated

slightly at every position. As for the stress in the middle of the graphene, all three stress formulations result in satisfactory uniform stress distribution (14.4 GPa), except that a slight overestimate is found in Lutsko's stress formulation.

3.4 Stress distribution in the graphene with covalent bond and vdW interaction

The local stress distribution in the graphene sheet with bonded and non-bonded interactions was also examined at both stress free state and uniaxial stress state. The variation of bond length at stress free state is shown in Fig. 3.4.1, in which ΔL represents the difference of bond length between graphene with and without free surfaces. It is obvious to see that the bonds at the surface are compressed while the others are elongated. Fig. 3.4.2 illustrates Hardy local stress distribution, from which, it is seen that the graphene sheet sustains compressive force in the vicinity of surfaces whereas in the middle, the graphene is under tensile loading. Besides, it is noted that near the surface, the stress increases slightly first and then drops gradually toward the surface, resulting in the distortion of configuration as found in Fig. 3.4.1. It is worthy to mention that even though the graphene does not posses zero stress at every position, the summation of stress from x=-35 to 35 along the x axis is still approximately zero at stress free state. Fig. 3.4.3 and 3.4.4 illustrate Lutsko and Tsai local stress distribution, respectively. From the figures, it is seen that the stress fluctuates substantially at every position; therefore, these two stress formulations are not suitable for describing the stress field when van der Waals is present.

Fig. 3.4.5 shows Hardy local stress distribution at uniaxial stress state of 10 GPa. Similarly, due to the difference of cross section area between the graphene sheet and simulation box, the actual load carried by graphene is 14.4 GPa. It is found that in the middle of the graphene, Hardy stress formulation results in accurate and uniform distribution; near the surface, the stress will drop gradually and the extent of

deduction and influence range are dependent on the form of localization function employed in Hardy stress expression. It can be seen that the bond length was elongated as shown in Fig. 3.4.6, due to the tensile stress existing at every position. Fig. 3.4.7 and 3.4.8 illustrate Lutsko and Tsai local stress distribution, respectively. From the figures, it is seen that the stress fluctuates substantially at every position; therefore, these two stress formulations are not suitable for describing the stress field when van der Waals is present.

Chapter 4 Graphene with central cracks subjected to uniaxial loading

This chapter aims to evaluate the local stress field of the graphene sheet with central cracks subjected to remote tensile loading numerically and theoretically, from which the fracture parameters can be deduced directly. In order to validate if the fracture parameters defined in continuum fracture mechanics are still applicable for atomistic structure, both the continuum and discrete models with the same geometry and crack lengths under prescribed loading were established, respectively. The continuum model and the corresponding stress field were obtained using finite element analysis (FEA), and the analytical LEFM [23] (linear elastic fracture mechanics) solution was also incorporated. For the discrete model, the atomistic structure was constructed through MD simulation, in which Hardy and Tsai stress formulations were employed to calculate the local stress distribution. For the purpose of describing the stress field in discrete model, the non-local elasticity [24] solution was introduced. Based on the results of stress distribution, the fracture parameters concerning the linkage between the continuum and atomistic structure were obtained.

In the following section, the non-local elasticity solution regarding the graphene with line crack under remote tensile loading was presented first. Subsequently, LEFM solutions as well as finite element analysis were compared and discussed. Next, the results of atomistic stress distribution in the equivalent discrete models were presented and compared with non-local elasticity solutions. Finally, the suitability of fracture parameters for characterizing the fracture behavior in atomistic structures was discussed.

4.1 Non-local elasticity in crack-tip problem

In classical elasticity, the solution of stress field in the line-crack problem of an elastic plate subject to remote uniform tension yields an infinite hoop stress at the

crack tip. In order to overcome the forward problem, Eringen [24] has proposed the non-local elasticity theory, in which the solution of stress field does not contain any singularity; instead, a finite hoop stress is found at the crack-tip such that the physical nature of the problem can be presented.

4.1.1 Near-tip stress field of non-local elasticity

The only difference between the non-local and classical elasticity is the constitutive equation and it is of the form

$$t_{kl}(\mathbf{r}) = \int_v \left[\lambda' e_{rr}(\mathbf{r}')\delta_{kl} + 2\mu' e_{kl}(\mathbf{r}') \right] dv(\mathbf{r}'), \tag{4.1.1}$$

where v is the volume occupied by the body, and λ' and μ' are non-local moduli and they are functions of the distance $|x'-x|$ between the reference point x and any other point x' in the body. For isotropic elastic solids, they are given by

$$(\lambda', \mu') = (\lambda, \mu)\alpha\left(|\mathbf{r}'-\mathbf{r}|\right), \tag{4.1.2}$$

where α is the kernel function and is optionally given. In this study, two types of kernel function will be considered: one is the triangular-shape distribution used in Eringen's paper and the other is the Gaussian function employed previously in Hardy's formulation. For the triangular-shape distribution, it is expressed as

$$\alpha\left(|\mathbf{r}'-\mathbf{r}|\right) = \begin{cases} K(a - |\mathbf{r}'-\mathbf{r}|), & |\mathbf{r}'-\mathbf{r}| \leq \mathbf{a} \\ 0, & |\mathbf{r}'-\mathbf{r}| \geq \mathbf{a} \end{cases} \tag{4.1.3}$$

where $K=3/\pi a^3$ for the 2-dimensional case and a is the lattice distance. For the Gaussian function, it is expressed as

$$\alpha(\mathbf{r'}-\mathbf{r}) = \frac{1}{(\sqrt{\pi}h)^2} \exp\left(-\frac{(\mathbf{r'}-\mathbf{r})^2}{h^2}\right),$$ (4.1.4)

where h is the smoothing length and is chosen to be 1.9 in this study. The two distributions were shown in Fig. 4.1.1. From eqn. (4.1.1), it is known that the stress $t_{kl}(\mathbf{r})$ at one point $\mathbf{r}$ depends on strains $e_{kl}(\mathbf{r'})$ at all points $\mathbf{r'} \in v$; as a result, the interactions with the surroundings $(\mathbf{r'})$ can be taken into account at the reference point $\mathbf{r}$. If the following classical Hook's law is introduced

$$\sigma_{kl}(\mathbf{r'}) \equiv \sigma'_{kl} = \lambda e'_{rr}(\mathbf{r'})\delta_{kl} + 2\mu e'_{kl}(\mathbf{r'}),$$ (4.1.5)

eqn. (4.1.1) can be expressed as

$$t_{kl}(\mathbf{r}) = \int_v \alpha(|\mathbf{r'}\text{-}\mathbf{r}|)\sigma_{kl}(\mathbf{r'})\, dv(\mathbf{r'}).$$ (4.1.6)

It is obvious to see that the stress at the point $\mathbf{r}$ is contributed from the stresses at other points $\mathbf{r'}$ in the body with appropriate weighting by the kernel function α. The equation of equilibrium with vanishing body force is

$$t_{kl,k}(\mathbf{r}) = \int_v \alpha(|\mathbf{r'}\text{-}\mathbf{r}|)\sigma_{kl,k}(\mathbf{r'})\, dv(\mathbf{r'}) = 0.$$ (4.1.7)

By employing the Green-Gauss theorem on eqn. (4.1.7), one can obtain the following

relation

$$\int_v \alpha\left(\|\mathbf{r'\text{-}r}\|\right)\sigma_{kl,k}(\mathbf{r'})dv(\mathbf{r'}) = \int_{\partial v} \alpha\left(\|\mathbf{r'\text{-}r}\|\right)\sigma_{kl}(\mathbf{r'})\,d\mathbf{A}(\mathbf{r'}),\qquad(4.1.8)$$

where ∂v is the boundary surface of the body v. It is noted that when the body extends to infinity or the surface tensions are negligible, the surface integral in eqn. (4.1.8) will vanish. As a result, the remaining becomes

$$\int_v \alpha\left(\|\mathbf{r'\text{-}r}\|\right)\sigma_{kl,k}(\mathbf{r'})\,dv(\mathbf{r'}) = 0.\qquad(4.1.9)$$

Since α is an arbitrary and continuous function, eqn. (4.1.9) is satisfied if and only if

$$\sigma_{kl,k}(\mathbf{r'}) = \mathbf{0}.\qquad(4.1.10)$$

Using the classical Hook's law of eqn. (4.1.5) and the following strain tensor

$$e_{kl}{}' \equiv e_{kl}(\mathbf{r'}) = \frac{1}{2}\left(u'_{k,l}+u'_{l,k}\right),\qquad(4.1.11)$$

one can obtain the following governing equations in 2-dimensinal problems

$$\begin{cases}(\lambda+\mu)\left(u'_{,x'x'}+v'_{,x'y'}\right)+\mu\nabla'^2 u'= 0\\ (\lambda+\mu)\left(u'_{,x'y'}+v'_{,y'y'}\right)+\mu\nabla'^2 v'= 0.\end{cases}\qquad(4.1.12)$$

Let the Fourier transform with respect to x defined as

24

$$\bar{f}(k,y) \equiv \frac{1}{\sqrt{2\pi}} \int_{-\infty}^{\infty} f(x,y)e^{ikx} dx, \tag{4.1.13}$$

then the Fourier transform of eqn. (4.1.12) with respect to x' gives the following equations

$$\begin{cases} -(\lambda + 2\mu)k^2\bar{u} + \mu\bar{u}_{,y'y'} - ik(\lambda + \mu)\bar{v}_{,y'} = 0 \\ -ik(\lambda + \mu)\bar{u}_{,y'} + (\lambda + 2\mu)\bar{v}_{,y'y'} - k^2\mu\bar{v} = 0, \end{cases} \tag{4.1.14}$$

where k is the variable in the transformed domain. For the above equations, the solutions of the displacement fields can be obtained [25]

$$u(x',y') = (2\pi)^{-1/2} \int_{-\infty}^{\infty} ik^{-1} \left[|k|A(k) + \left(|k|y' - \frac{\lambda + 3\mu}{\lambda + \mu} \right)B(k) \right] \exp(-|k|y' - ikx')dk$$

$$v(x',y') = (2\pi)^{-1/2} \int_{-\infty}^{\infty} \left[A(k) + y'B(k) \right] \exp(-|k|y' - ikx')dk \tag{4.1.15}$$

where $A(k)$ and $B(k)$ are two functions to be determined from the boundary conditions (Fig. 4.1.2)

$$t_{yx} = \sigma_{yx} = 0 \qquad y = 0 \qquad \forall \mathbf{x} \tag{4.1.16}$$

$$t_{yy} = -t_0 \qquad y = 0 \qquad |\mathbf{x}| < L \tag{4.1.17}$$

$$v = 0 \qquad y = 0 \qquad |\mathbf{x}| > L. \tag{4.1.18}$$

From eqn. (4.1.16), one can obtain the following equation

$$\sigma_{yx}(x',0) = (2\pi)^{-1/2} \int_{-\infty}^{\infty} \mu\, i \exp(-ikx') \left[-2kA(k) + B(k)\left(1 + \frac{\lambda + 3\mu}{\lambda + \mu}\right) \right] dk = 0. \quad (4.1.19)$$

Therefore, based on the above relation, $B(k)$ can be expressed in terms of $A(k)$ as

$$B(k) = \left(\frac{\lambda + \mu}{\lambda + 2\mu}\right) kA(k). \quad (4.1.20)$$

The displacement fields then can be expressed as

$$u(x',y') = -\left(\frac{2}{\pi}\right)^{1/2} \frac{(\lambda + \mu)}{(\lambda + 2\mu)} \int_{0}^{\infty} A(k)(\frac{\mu}{\lambda + \mu} - ky') \exp(-ky') \sin(x'k)\, dk \quad (4.1.21)$$

$$v(x',y') = \left(\frac{2}{\pi}\right)^{1/2} \frac{(\lambda + \mu)}{(\lambda + 2\mu)} \int_{0}^{\infty} A(k)(\frac{\mu + 2\mu}{\lambda + \mu} + ky') \exp(-ky') \cos(x'k)\, dk. \quad (4.1.22)$$

The remaining two boundary conditions is used to determine the unknown function $A(k)$. From eqn. (4.1.15),

$$t_{yy} = \int_{-\infty}^{\infty} \int_{-\infty}^{\infty} \alpha(|x'-x|,|y'-y|)\sigma_{yy}(x',y')\, dx'\, dy'$$

$$= \int_{0}^{\infty} \int_{-\infty}^{\infty} \sigma_{yy}(x',y')\left[\alpha(|x'-x|,|y'-y|) + \alpha(|x'-x|,|y'+y|)\right] dx'\, dy' \quad (4.1.23)$$

$$= -t_0,$$

where σ_{yy} is expressed as

$$\sigma_{yy}(x',y') = -2\left(\frac{2}{\pi}\right)^{1/2} \frac{\mu(\lambda + \mu)}{(\lambda + 2\mu)} \int_{0}^{\infty} kA(k)(1 + ky') \exp(-ky') \cos(x'k)\, dk. \quad (4.1.24)$$
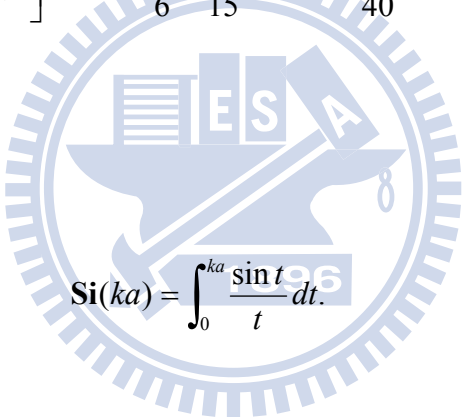
26

It is noted that for the triangular-shape distribution curve, Eringen showed the result of the integration, i.e. eqn. (4.1.23) as the following

$$t_{yy} = \left(\frac{2}{\pi}\right)^{1/2} \frac{2\mu(\lambda + \mu)}{(\lambda + 2\mu)} \int_0^\infty kA(k)\cos(xk)\overline{\alpha}(ka)\, dk = t_0, \qquad (4.1.25)$$

where $\overline{\alpha}$ is expressed as

$$\overline{\alpha}(ka) = -\frac{6}{\pi}\left\{\left[\frac{13}{30}(ka)^{-1} + \frac{32}{15}(ka)^{-3} - \frac{1}{20}(ka)\right]\cos(ka) + \left[\frac{19}{30}(ka)^{-2} - \frac{1}{20}\right]\sin(ka)\right.$$
$$\left. + \left[\frac{1}{3} - \frac{1}{20}(ka)^2\right]\mathbf{Si}(ka) - \frac{\pi}{6} - \frac{32}{15}(ka)^{-3} + \frac{\pi}{40}(ka)^2\right\}$$

with

$$\mathbf{Si}(ka) = \int_0^{ka} \frac{\sin t}{t}\, dt.$$

For the Gaussian kernel function, the exact solution of the integration can be obtained and the detail of the derivation will be shown in the following. The boundary condition of eqn. (4.1.17) is shown again

$$t_{yy} = \int_0^\infty \int_{-\infty}^\infty \sigma_{yy}(x', y')\left[\alpha\left(|x'-x|, |y'-y|\right) + \alpha\left(|x'-x|, |y'+y|\right)\right] dx'\, dy' = -t_0 \qquad (4.1.26)$$

where

$$\sigma_{yy}(x',y') = -2\left(\frac{2}{\pi}\right)^{1/2}\frac{\mu(\lambda+\mu)}{(\lambda+2\mu)}\int_0^\infty kA(k)(1+ky')\exp(-ky')\cos(x'k)dk \quad (4.1.27)$$

$$\alpha = \frac{1}{\pi}p\exp\left\{-p\left[(x'-x)^2+(y'-y)^2\right]\right\} \quad \textbf{with} \quad p = \left(\frac{1}{h}\right)^2.$$

By introducing eqn. (4.1.27) into eqn. (4.1.26), one can obtain

$$\begin{aligned}
t_{yy} = \int_0^\infty\int_{-\infty}^\infty\int_0^\infty & -2\left(\frac{2}{\pi}\right)^{1/2}\frac{\mu(\lambda+\mu)}{(\lambda+2\mu)}kA(k)(1+ky')\exp(-ky')\cos(x'k) \\
& \times\frac{1}{\pi}p\exp\left\{-p\left[(x'-x)^2+(y'-y)^2\right]\right\}dx'dy'dk + \\
\int_0^\infty\int_{-\infty}^\infty\int_0^\infty & -2\left(\frac{2}{\pi}\right)^{1/2}\frac{\mu(\lambda+\mu)}{(\lambda+2\mu)}kA(k)(1+ky')\exp(-ky')\cos(x'k) \\
& \times\frac{1}{\pi}p\exp\left\{-p\left[(x'-x)^2+(y'+y)^2\right]\right\}dx'dy'dk.
\end{aligned} \quad (4.1.28)$$

For the first term of eqn. (4.1.28), if the integration with respect to x' is performed first, it can be rearranged as

$$\begin{aligned}
\int_0^\infty\int_{-\infty}^\infty\int_0^\infty & -2\left(\frac{2}{\pi}\right)^{1/2}\frac{\mu(\lambda+\mu)}{(\lambda+2\mu)}kA(k)(1+ky')\exp(-ky')\cos(x'k) \\
& \times\frac{1}{\pi}p\exp\left\{-p\left[(x'-x)^2+(y'-y)^2\right]\right\}dx'dy'dk \\
= \int_0^\infty\int_0^\infty & (-2)\frac{p}{\pi}\left(\frac{2}{\pi}\right)^{1/2}\frac{\mu(\lambda+\mu)}{(\lambda+2\mu)}kA(k)(1+ky')\exp(-ky')\exp\left[-p(y'-y)^2\right] \\
& \times\left\{\cos(kx')\exp\left[-p(x'-x)^2\right]dx'\right\}dy'dk
\end{aligned} \quad (4.1.29)$$

Using the following integral relation [26]

$$I_1 = \int_{-\infty}^{\infty} \exp(-Px'^2) \cos \xi (x + x') dx' = (\frac{\pi}{P})^{1/2} \exp(-\frac{\xi^2}{4p}) \cos(\xi x), \qquad (4.1.30)$$

one can obtain the following equation

$$\int_{-\infty}^{\infty} \cos(kx') \exp\{- p(x'-x)^2 \} dx' = \left(\frac{\pi}{p}\right)^{1/2} \exp(-\frac{k^2}{4p}) \cos(kx). \qquad (4.1.31)$$

As a result, eqn. (4.1.29) can be expressed as

$$\int_0^{\infty} \int_0^{\infty} (-2) \frac{p}{\pi} \left(\frac{2}{\pi}\right)^{1/2} \frac{\mu(\lambda + \mu)}{(\lambda + 2\mu)} kA(k)(1 + ky') \exp(-ky') \exp\left[- p(y'-y)^2\right]$$
$$\times \left\{ \cos(kx') \exp\left[- p(x'-x)^2\right] dx' \right\} dy' dk$$
$$= \int_0^{\infty} \int_0^{\infty} (-2) \frac{p}{\pi} \left(\frac{2}{\pi}\right)^{1/2} \frac{\mu(\lambda + \mu)}{(\lambda + 2\mu)} kA(k)(1 + ky') \exp(-ky') \exp\left[- p(y'-y)^2\right] \qquad (4.1.32)$$
$$\times \left\{ \left(\frac{\pi}{p}\right)^{1/2} \exp(-\frac{k^2}{4p}) \cos(kx) \right\} dy' dk$$

If the integration with respect to y' is performed next, eqn. (4.1.32) can be rearranged

as

$$\int_0^{\infty} \int_0^{\infty} (-2) \frac{p}{\pi} \left(\frac{2}{\pi}\right)^{1/2} \frac{\mu(\lambda + \mu)}{(\lambda + 2\mu)} kA(k)(1 + ky') \exp(-ky') \exp\left[- p(y'-y)^2\right]$$
$$\times \left\{ \left(\frac{\pi}{p}\right)^{1/2} \exp(-\frac{k^2}{4p}) \cos(kx) \right\} dy' dk$$
$$\qquad (4.1.33)$$
$$= \int_0^{\infty} -\left(\frac{2}{\pi}\right)^{1/2} \frac{2p\mu(\lambda + \mu)}{\pi(\lambda + 2\mu)} \left(\frac{\pi}{p}\right)^{1/2} kA(k) \cos(xk) \exp(-\frac{k^2}{4p})$$
$$\times \left\{ \int_0^{\infty} (1 + ky') \exp\{- p[(y'-y)^2] - ky'\} dy' \right\} dk \, .$$

where

$$\int_0^\infty (1+ky')\exp\{-p[(y'-y)^2]-ky'\}\,dy'$$

$$= \int_0^\infty \exp\{-py'^2-(k-2py)y'\}\,dy'\,\exp(-py^2)+\int_0^\infty y'\exp\{-py'^2-(k-2py)y'\}\,dy'\,\exp(-py^2)k\ .$$

Using the following integral relations [26]

$$I_2 = \int_0^\infty \exp(-Py'^2-\xi y')dy'=\frac{1}{2}(\frac{\pi}{P})^{1/2}\exp(\frac{\xi^2}{4p})\left[1-\phi(\frac{\xi}{2\sqrt{P}})\right] \qquad (4.1.34)$$

$$I_3 = \int_0^\infty y'\exp(-Py'^2-\xi y')dy'=\frac{1}{2P}-\frac{\xi}{4P}(\frac{\pi}{P})^{1/2}\exp(\frac{\xi^2}{4p})\left[1-\phi(\frac{\xi}{2\sqrt{P}})\right] \qquad (4.1.35)$$

with

$$\phi(z)=2\pi^{-1/2}\int_0^z \exp(-t^2)dt$$

one can obtain the following equations

$$\int_0^\infty \exp\{-py'^2-(k-2py)y'\}\,dy'\,\exp(-py^2)$$

$$= \exp(-py^2)\left\{\frac{1}{2}\left(\frac{\pi}{p}\right)^{1/2}\exp(\frac{(k-2py)^2}{4p})\left[1-\phi(\frac{k-2py}{2\sqrt{p}})\right]\right\} \qquad (4.1.36)$$

$$\int_0^\infty y'\exp\{-py'^2-(k-2py)y'\}\,dy'\,\exp(-py^2)k$$

$$= \exp(-py^2)\left\{\frac{k}{2p}-\frac{k(k-2py)}{4p}\left(\frac{\pi}{p}\right)^{1/2}\exp(\frac{(k-2py)^2}{4p})\left[1-\phi(\frac{k-2py}{2\sqrt{p}})\right]\right\}. \qquad (4.1.37)$$

If eqn. (4.1.36) and eqn. (4.1.37) are introduced into eqn. (4.1.33), then eqn. (4.1.33) can be expressed as

$$\int_0^\infty -\left(\frac{2}{\pi}\right)^{1/2}\frac{2p\mu(\lambda+\mu)}{\pi(\lambda+2\mu)}\left(\frac{\pi}{p}\right)^{1/2}kA(k)\cos(xk)\exp(-\frac{k^2}{4p})$$

$$\times\left\{\int_0^\infty (1+ky')\exp\left\{-p\left[(y'-y)^2\right]-ky'\right\}dy'\right\}dk$$

$$=\int_0^\infty -\left(\frac{2}{\pi}\right)^{1/2}\frac{2p\mu(\lambda+\mu)}{\pi(\lambda+2\mu)}\left(\frac{\pi}{p}\right)^{1/2}kA(k)\cos(xk)\exp(-\frac{k^2}{4p})$$

$$\times\left\{\exp(-py^2)\left\{\left(\frac{\pi}{p}\right)^{1/2}\exp(\frac{(k-2py)^2}{4p})\left[1-\phi(\frac{k-2py}{2\sqrt{p}})\right]\left[\frac{1}{2}-\frac{k(k-2py)}{4p}\right]+\frac{k}{2p}\right\}\right\}dk.$$

(4.1.38)

Similarly for the second term of eqn. (4.1.28), it can be obtained as

$$\int_0^\infty\int_{-\infty}^\infty\int_0^\infty -2\left(\frac{2}{\pi}\right)^{1/2}\frac{\mu(\lambda+\mu)}{(\lambda+2\mu)}kA(k)(1+ky')\exp(-ky')\cos(x'k)$$

$$\times\frac{1}{\pi}p\exp\left\{-p\left[(x'-x)^2+(y'+y)^2\right]\right\}dx'dy'dk$$

$$=\int_0^\infty -\left(\frac{2}{\pi}\right)^{1/2}\frac{2p\mu(\lambda+\mu)}{\pi(\lambda+2\mu)}\left(\frac{\pi}{p}\right)^{1/2}kA(k)\cos(xk)\exp(-\frac{k^2}{4p})$$

$$\times\exp(-py^2)\left\{\left(\frac{\pi}{p}\right)^{1/2}\exp(\frac{(k+2py)^2}{4p})\left[1-\phi(\frac{k+2py}{2\sqrt{p}})\right]\left[\frac{1}{2}-\frac{k(k+2py)}{4p}\right]+\frac{k}{2p}\right\}dk.$$

(4.1.39)

Now with y=0, the boundary condition of eqn. (4.1.39) can be expressed as

31

$t_{yy}(x,0)$

$$= -\left(\frac{2}{\pi}\right)^{1/2} \frac{2p\mu(\lambda+\mu)}{\pi(\lambda+2\mu)}\left(\frac{\pi}{p}\right)\int_0^\infty kA(k)\cos(xk)\left\{\left[1-\phi(\frac{k}{2\sqrt{p}})\right]\left[1-\frac{k^2}{2p}\right]+\frac{k}{\sqrt{\pi p}}\exp(-\frac{k^2}{4p})\right\}dk$$

$$= -\left(\frac{2}{\pi}\right)^{1/2} \frac{2\mu(\lambda+\mu)}{(\lambda+2\mu)}\int_0^\infty kA(k)\cos(xk)\left\{[1-\phi(\varepsilon k)][1-2(\varepsilon k)^2]+\frac{2(\varepsilon k)}{\sqrt{\pi}}\exp(-(\varepsilon k)^2)\right\}dk$$

$$= -t_0$$

(4.1.40)

with

$$\varepsilon = \frac{1}{2\sqrt{P}}.$$

For the purpose of making the above equation more brevity, one can rewritten eqn, (4.1.40) as

$$t_{yy}(x,0) = -\left(\frac{2}{\pi}\right)^{1/2} \frac{2\mu(\lambda+\mu)}{(\lambda+2\mu)}\int_0^\infty kA(k)\cos(xk)\overline{\alpha}(\varepsilon k)dk = -t_0 \qquad |\mathbf{x}| < L \quad (4.1.41)$$

where

$$\overline{\alpha}(\varepsilon k) = \left\{[1-\phi(\varepsilon k)][1-2(\varepsilon k)^2]+\frac{2(\varepsilon k)}{\sqrt{\pi}}\exp(-(\varepsilon k)^2)\right\}.$$

It is worth to mention that the only difference between eqn. (4.1.40) and Eringen's result is in the form of $\overline{\alpha}$. Therefore, it is interesting to see the difference of stress distribution with two different types of kernel functions. The other boundary condition eqn. (4.1.18) gives

$$v(x,0) = \int_0^\infty A(k)\cos(xk)dk = 0 \qquad |\mathbf{x}| > L \qquad\qquad (4.1.42)$$

As a consequence, the two boundary conditions lead to a pair of dual integral equations, eqn. (4.1.41) and eqn. (4.1.42), which must be solved to determine A(k). The only difference between the non-local elasticity and classical elasticity is in the introduction of the function $\bar{\alpha}$. For the classical elasticity in the same crack-tip problem, the boundary conditions are

$$\sigma_{yx} = 0, \qquad y = 0 \qquad \forall \mathbf{x} \qquad\qquad (4.1.43)$$

$$\sigma_{yy} = -t_0, \qquad y = 0 \qquad |\mathbf{x}| < L \qquad\qquad (4.1.44)$$

$$v = 0, \qquad y = 0 \qquad |\mathbf{x}| > L. \qquad\qquad (4.1.45)$$

The only difference is the eqn. (4.1.44), which is expressed as

$$\sigma_{yy}(x,0) = -\left(\frac{2}{\pi}\right)^{1/2} \frac{2\mu(\lambda+\mu)}{(\lambda+2\mu)} \int_0^\infty kA(k)\cos(xk)dk = -t_0. \qquad\qquad (4.1.46)$$

As a result, the dual integral equations of classical elasticity satisfying eqn. (4.1.44) and (4.1.45) are found to be [25]

$$\int_0^\infty KA(K)\cos(\bar{x}K)\,dK = 1 \qquad |\bar{\mathbf{x}}| < 1 \qquad\qquad (4.1.47)$$

$$\int_0^\infty A(K)\cos(\bar{x}K)dK = 0 \qquad |\bar{\mathbf{x}}| > 1, \qquad\qquad (4.1.48)$$

with

33

$$K = kL, \quad \bar{x} = \frac{x}{L}$$

$$A(K) = \left(\frac{2}{\pi}\right)^{1/2} \left[\frac{2\mu(\lambda + \mu)}{L^2 t_0 (\lambda + 2\mu)}\right] A(k).$$

The solution of $A(K)$ in the eqn. (4.1.47) and (4.1.48) has been obtained [25] as

$$A(K) = \frac{J_1(K)}{K}, \tag{4.1.49}$$

where J_1 is the Bessel function of the first kind of order one. Eringen has demonstrated the applicability of utilizing the classical displacement field to calculate the non-local stress field in his work. For the purpose of introducing the above classical elasticity solution into the non-local elasticity, the dual integral equations of non-local elasticity, i.e. eqn. (4.1.41) and eqn. (4.1.42), are rewritten as

$$\int_0^\infty KA(K)\cos(\bar{x}K)\,\bar{\alpha}(\varepsilon\frac{K}{L})\,dK = 1 \qquad |\bar{\mathbf{x}}| < 1 \tag{4.1.50}$$

$$\int_0^\infty A(K)\cos(\bar{x}K)\,dK = 0 \qquad\qquad |\bar{\mathbf{x}}| > 1 \tag{4.1.51}$$

with

$$K = kL, \quad \bar{x} = \frac{x}{L}$$

$$A(K) = \left(\frac{2}{\pi}\right)^{1/2} \left[\frac{2\mu(\lambda + \mu)}{L^2 t_0 (\lambda + 2\mu)}\right] A(k).$$

By employing eqn. (4.1.49) into eqn. (4.1.50), the non-local stress field can be

obtained as

$$\frac{t_{yy}}{t_0} = \int_0^\infty J_1(K)\cos(\bar{x}K)\,\bar{\alpha}(\varepsilon\frac{K}{L})\,dK.$$ (4.1.52)

It is worthy to mention that Eringen's method of introducing classical solution into non-local elasticity stress field cannot fully satisfy the boundary condition. The normal stress boundary condition $t_{yy}(x,0) = -t_0$ for $|x| < L$ is satisfied in an approximate sense. One way to obtain the solution that fully satisfies the normal stress boundary condition can be found in Zhou et al [27]. In their work, they proposed Schmidt's method to solve the dual boundary conditions. However, it was found that the maximum stress position is far away from the crack tip in the current study, as shown in Fig. 4.1.4; therefore, Eringen's approach was adopted in this paper. Similarly, for triangular-shape kernel function, the dual integral equations are

$$\left(\frac{2}{\pi}\right)^{1/2}\frac{2\mu(\lambda+\mu)}{(\lambda+2\mu)}\int_0^\infty kA(k)\cos(xk)\bar{\alpha}(ka)dk = t_0$$ (4.1.53)

$$v(x,0) = \int_0^\infty A(k)\cos(xk)dk = 0$$ (4.1.54)

where $\bar{\alpha}$ is expressed as

$$\bar{\alpha}(ka) = -\frac{6}{\pi}\left\{\left[\frac{13}{30}(ka)^{-1} + \frac{32}{15}(ka)^{-3} - \frac{1}{20}(ka)\right]\cos(ka) + \left[\frac{19}{30}(ka)^{-2} - \frac{1}{20}\right]\sin(ka)\right.$$
$$\left. + \left[\frac{1}{3} - \frac{1}{20}(ka)^2\right]\mathbf{Si}(ka) - \frac{\pi}{6} - \frac{32}{15}(ka)^{-3} + \frac{\pi}{40}(ka)^2\right\}$$

Since the method of introducing classical elasticity solution is independent of the form of $\bar{\alpha}$, eqn. (4.1.53) and (4.1.54) can be rewritten as

$$\int_0^\infty KA(K)\cos(\bar{x}K)\,\bar{\alpha}(a\frac{K}{L})\,dK = 1 \qquad |\bar{x}| < 1 \qquad (4.1.55)$$

$$\int_0^\infty A(K)\cos(\bar{x}K)\,dK = 0 \qquad\qquad |\bar{x}| > 1 \qquad (4.1.56)$$

with

$$K = kL, \qquad \bar{x} = \frac{x}{L}$$

$$A(K) = \left(\frac{2}{\pi}\right)^{1/2}\left[\frac{2\mu(\lambda+\mu)}{L^2 t_0(\lambda+2\mu)}\right]A(k) = \frac{J_1(K)}{K}.$$

The stress field then can be obtained as

$$\frac{t_{yy}}{t_0} = \int_0^\infty J_1(K)\cos(\bar{x}K)\,\bar{\alpha}(a\frac{K}{L})\,dK. \qquad (4.1.57)$$

It is noted that the stress field with Gaussian function (4.1.52) is identical in form to (4.1.57), except that the kernel function $\bar{\alpha}$ employed is different. By superimposing t_0 on the stress fields, one can obtain the solution of the line-crack problem, in which the crack surface is free of traction whereas a uniform tension t_0 is exerting on the plate at $y=\infty$ (Fig. 4.1.3). Accordingly, the near-tip stress field is expressed as

$$t(x,0) = t_{yy}(x,0) + t_0. \qquad (4.1.58)$$

4.1.2 Comparison of non-local stress fields with different distribution curves

In this subsection, the non-local elasticity stress fields with two different kernel functions, i.e. triangular and Gaussian function were compared and discussed. The lattice length of the graphene is 2.46 Å and the remote tensile loading is 2 GPa. Fig. 4.1.5 to 4.1.7 show the stress distribution near the crack tip with crack lengths equal to 3 lattices, 41 lattices, and 81 lattices, respectively. It is apparent to see that for all the crack lengths, the near-tip stress exhibits finite value instead of singularity at the crack tip, and the position of the maximum stress is slightly ahead of the tip within one lattice. With different kernel functions, the value and the position of the maximum stress shows some difference. The maximum stress obtained from triangular function is larger than the one with Gaussian function, and the position is slightly closer to the crack tip. Around one lattice away from the crack tip, the two stress fields coincides with each other and converges to unity. Based on the above results, it is demonstrated that the non-local elasticity theory can overcome the problem of singularity and the maximum stress position is close to the crack tip; therefore it is an effective approach to investigate the physical nature of crack problems. For the comparing purpose, the non-local elasticity solution with Gaussian function is adopted in the following discussion, since it is also employed in Hardy's stress formulation.

4.2 Comparison of stress fields in continuum models

The continuum graphene and the stress field were obtained through finite element analysis (FEA). Fig. 4.2.1 and Table 4.2.1 show the dimension of the three models with crack lengths of 3 lattices, 41 lattices, and 81 lattices, respectively. It is noted that the width of the graphene (2W) is ten times larger than the crack length and the corresponding height (2H) is around the same with the width. Because of symmetry, only one quadrant of the model was used. The dotted lines in Fig. 4.2.1

illustrate the representative volume elements (RVE) for the FEA. The material properties utilized in the FEA model were calculated based on the molecular dynamic simulation with the interatomistic energy described earlier, and the results are presented in Table 4.2.2. All the FEA results are obtained using finite element code ANSYS with four-node element (plane 42) applied in all cases. To ensure that the singularity stress field can be precisely simulated, a fine mesh is used near the crack tip, where the spacing between the nodes along the crack axis (y=0) is small enough with respect to crack length. A representative finite element model for crack lengths of 41 lattices is shown in Fig. 4.2.2. It is worthy to mention that the element size in the fine mesh is maintained uniform before and ahead of the crack tip and the ratio between crack size and element size is larger than 300 for all the cases. The remote tensile loading 2 GPa in the y direction was applied on the graphene sheet. In addition to finite element analysis, LEFM is an alternative approach to calculate the stress field in continuum models. For a finite plate with a central crack, the stress field can be obtained as [23]

$$\sigma_{yy} = \frac{K}{\sqrt{2\pi x}} \tag{4.2.1}$$

where x is the distance from the crack tip along the crack axis. The stress intensity factor K can be approximated in a polynomial form [23] as

$$K = \sigma_0 \sqrt{\pi L} \left[\sec\left(\frac{\pi L}{2W}\right)^{1/2} \right]\left[1 - 0.025\left(\frac{L}{W}\right)^2 + 0.06\left(\frac{L}{W}\right)^4 \right] \tag{4.2.2}$$

where σ_0 is the remote loading acting on the graphene sheet, L is the half crack

length and W is the half graphene width.

Fig. 4.2.3 to 4.2.5 show the stress distribution near the crack tip obtained from FEA and LEFM. It is apparent to see that for all the crack lengths, the stress field in continuum models demonstrates $1/\sqrt{x}$ stress singularity near the crack tip. Moreover, it was found that for small crack lengths such as 3 lattices, the LEFM solution deviated from the FEM solution at the position slightly away from the tip. It is known that when the position is far way from the crack tip, the stress field should be equal to the remote applied loading. It is found, however, that for the crack lengths of 3 lattices, the stress field of LEFM is below unity when the position is one lattice away from the crack tip. With the increase of crack lengths, the LEFM solution was closer to the FEM solution. For crack lengths of 41 lattices, the LEFM solution deviated from the FEM solution at the position around one lattice from the tip; for crack lengths of 81 lattices, the LEFM solution was approximately in agreement with the FEM solution. Based on the above results, it is demonstrated that the use of LEFM solutions to describe the stress field with small crack length is not suitable; this result was also obtained by Sun et al [28]. On the other hand, FEM solution is applicable for describing the stress field with various crack lengths, even for crack length of few lattices.

4.3 Comparison of stress fields in discrete models

The atomistic structure of single layer graphene sheet under uniaxial loading was constructed through molecular dynamic simulation. Followed by the procedures mentioned in Chapter 2, the atomistic structure of graphene sheet with a uniaxial stress state of 2 GPa was obtained by performing the modified NPT ensemble. The central crack of length 2L in the graphene sheet was created by eradicating the associated covalent bond so that for the atom pairs across the crack surface, there was

no atomistic interaction occurring, as illustrated in Fig. 4.3.1. It is noted that due to the fact the non-bonded interaction exhibits less contribution to the mechanical properties of graphene sheet as compared to the covalent bond, van der Waals interaction is neglected in the current atomistic models. After the graphene sheet achieved the stress state of 2 GPa, Hardy stress formulation with h=1.9 and R_c=10 and Tsai stress formulation with dividing area 3.4×2.46 Å were adopted to calculate the stress distribution. In order to determine the size of the graphene model such that the geometry would not affect the result, the graphene with central cracks of 5 lattices and three different widths were discussed first. The dimensions of the models with three different widths are listed in Table 4.3.1 and the corresponding Hardy stress distribution is shown in Fig. 4.3.2. It is clear to see that when the graphene width is ten times larger than the crack length, the stress distributions are about the same. As a result, for the discrete models, the width of the graphene (2W) is chosen to be ten times of the crack length and the corresponding height (2H) is around the same with the width. The dimension of the graphene sheet with different cracks lengths considered in discrete models is shown in Table 4.3.2.

Fig. 4.3.3 to 4.3.11 show the stress distribution near the crack tip obtained from Hardy stress, Tsai stress and non-local elasticity solution. It is apparent to see that the stress fields obtained in the discrete models deviate from the $1/\sqrt{x}$ singularity solution near the crack tip and exhibit finite value. The maximum stress obtained from Hardy's formulation is in agreement with the non-local elasticity solution, whereas Tsai stress shows less agreement and is larger than the non-local elasticity solution, as shown in Table 4.3.3 and Fig. 4.3.12. As a result, it is indicated that the expression of Hardy stress exhibits non-local attribute within about one lattice from the crack tip. From Fig. 4.3.12, it is also found that with the increase of crack lengths, the maximum stress will increase accordingly. This attribute is similar to the result of LEFM that the

stress intensity factor will increase with the increase of crack lengths, except that the result can be deduced directly from maximum stress without other extraneous consideration. The stress distribution diagrams shown in Fig. 4.3.3 to 4.3.11 also illustrate that the position of maximum stress obtained from Hardy's formula is closer to the crack tip, compared to the non-local elasticity theory; in other words, Hardy stress can more effectively exhibit the stress field near the crack tip in terms of the maximum stress position, where supposed to be the crack tip. Though the maximum stress position obtained from Tsai's formulation is exactly at the crack tip, however, the maximum stress is larger than non-local elasticity solution. In addition, it was found that due to the limitation that the dividing plane mush be located at the position where the interaction force acting, the local stress distribution of Tsai's formulation shows less smoothness near the crack tip. Therefore, only Hardy stress field was suitable for investigating the fracture properties directly from maximum stress hypothesis. The results would be compared with the non-local elasticity solution and the discussion was presented in the following section.

4.4 Characterizing the fracture properties of graphene sheet

Based on the calculation of Hardy stress field and non-local elasticity solutions, the fracture properties of the graphene sheet with various crack lengths can be characterized directly from maximum stress hypothesis. The purpose of the study is to validate if the fracture parameters defined in continuum fracture mechanics, such as stress intensity factor and fracture toughness, are still applicable to atomistic structure, thus being able to bridge the gaps between the discrete and continuum models of graphene sheet.

4.4.1 Stress intensity factor K

The stress intensity factor of the continuum solid can be determined from the near-tip stress field [23] as

$$K_I = \lim_{x \to 0} \sqrt{2\pi x}\, \sigma_{yy} \qquad (4.4.1)$$

where σ_{yy} is the tensile stress component near the crack tip and x is the distance from the crack tip along the crack axis. For the continuum models, σ_{yy} is singular near the crack tip (x=0) and K_I is usually determined by the projection based on the converged values of $\sqrt{2\pi x}\, \sigma_{yy}$ at a distance from the crack tip. For the discrete models, the same projection approach was employed in the Hardy stress field to obtain the corresponding stress intensity factor. Fig. 4.4.1 to 4.4.3 demonstrate the $\sqrt{2\pi x}\, \sigma_{yy}$ plot with the projection and the actual solution $K_I = \sigma_0 \sqrt{\pi L}$ for the 3 models, crack lengths of 3 lattices, 41 lattices, and 81 lattices, respectively. The projected K_I is also listed in Table 4.4.1. It is found that for all the crack lengths, the stress intensity factor obtained from FEA was in agreement with the actual solution and it would increase with the increase of crack lengths. As a result, the projection method based on the converged value of $\sqrt{2\pi x}\, \sigma_{yy}$ is an effective approach to characterize the stress intensity factor. For the discrete model, the stress intensity factor obtained from Hardy stress field was also close to the FEA and the actual solution. Though the value is slightly lower than the others, the difference is small for all the crack lengths. Therefore, the stress intensity factor is able to characterize the stress field near the crack tip effectively for both the continuum and discrete models.
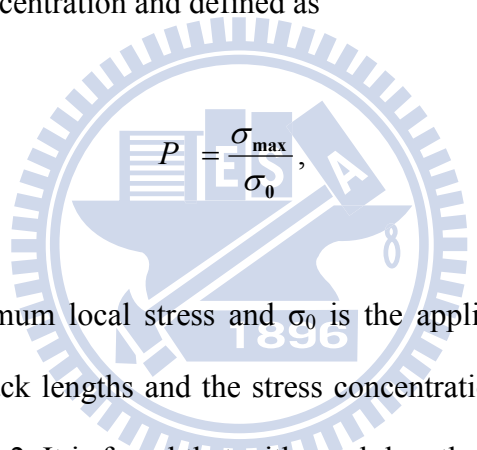
4.4.2 Fracture toughness K_{IC}

In fracture mechanics, the fracture toughness in a continuum solid is a material property which should be independent of crack lengths in the continuum model. In order to obtain the fracture toughness in the discrete model, the stress concentration factor defined by Eringen et al. [24] is introduced and expressed as

$$C = \left(\frac{2L}{a}\right)^{-1/2} P \qquad (4.4.2)$$

where P is the stress concentration and defined as

$$P = \frac{\sigma_{max}}{\sigma_0},$$

where σ_{max} is the maximum local stress and σ_0 is the applied remote loading. The relation between the crack lengths and the stress concentration factor can be seen in Fig. 4.4.4. and Table 4.4.2. It is found that with crack lengths less than 40 lattices, the stress concentration factor is dependent of the crack length. The shorter the crack length is, the higher the stress concentration will be. With crack lengths over 40 lattices, it can be seen that the stress concentration is approaching a constant. For Hardy's formula, the value is approaching 0.66, which is close to the non-local elasticity solution 0.64. It is known that if the maximum local stress achieves the cohesive strength, the fracture of the covalent bond will occur. In this condition, σ_{max} is equivalent to the cohesive strength σ_c, so eqn. (4.4.2) can be expressed as

$$\sigma_0 = \frac{1}{C}\left(\frac{2L}{a}\right)^{-1/2} \sigma_c. \qquad (4.4.3)$$

For the purpose of convenience in calculation, the cohesive strength σ_c is assumed to be 1 GPa in the following discussion. The relation between the applied loading with different crack lengths is shown in Fig. 4.4.5 and Table 4.4.3. It is found that with shorter crack lengths, the required loading is higher than those with larger crack lengths. In other words, the graphene sheets with short crack lengths are more resistant to crack extension than those with larger crack lengths. According to the above discussion that the stress intensity factor for the graphene atomistic structures is equal to $K_I = \sigma_0 \sqrt{\pi L}$, combination of eqn.(4.4.2) yields to the stress intensity factor as

$$K = (\pi L)^{1/2} \sigma_0 = (\pi L)^{1/2} \frac{1}{C} \left(\frac{a}{2L} \right)^{1/2} \sigma_{max}, \tag{4.4.4}$$

If the local maximum stress σ_{max} achieves the cohesive strength, the fracture toughness is derived as

$$K_{IC} = \frac{1}{C} \left(\frac{a\pi}{2} \right)^{1/2} \sigma_c. \tag{4.4.5}$$

The relation between the fracture toughness and different crack lengths is shown in Fig. 4.4.6. and Table 4.4.4. It is apparent that when the crack length is larger than 40 lattices, the fracture toughness is approaching a constant. For Hardy's formula, the value is approaching 2.97, which is closed to the non-local elasticity solution 3.10. It is found, however, that for the crack length less than 40 lattices, the fracture toughness is dependent of the crack length. The smaller the crack length is, the lower

the fracture toughness will be. Therefore, it is demonstrated that the fracture toughness may not be a material constant when the crack length is less than 40 lattices. The similar result was also obtained by Sun. et al. [28] who indicated that the fracture toughness of NaCl system is relied on the crack length as the crack is small (below 40 Å).

Chapter 5 Conclusion

Hardy local stress formulation was employed successfully to calculate the local stress distribution of the graphene sheet with free surface and central cracks. Based on the local stress distribution, the local properties of graphene sheet with presence of free surface and cracks were determined. Results indicated that for the graphene with free surfaces, when van der Waals force is present, the bond length at the edge is shortened; therefore the edge of the graphene sustains compressive stress. However, when van der Waals force is absent, the bond length in the whole atomistic graphene structure is remaining constant and therefore there is no stress induced on the atomistic structure. Moreover, the local stress distribution near the free surface of the graphene can be characterized successfully using Hardy stress formulation which exactly exhibits the local deformation of the microstructures within the graphene sheet.

With regard to the graphene with central cracks subjected to remote uniaxial loading, it was observed that for continuum models, both FEA and LEFM solution yield stress singularity near the crack tip. In addition, for small cracks, LEFM solution would deviate from the FEA. For discrete models, it was found that Hardy stress formulation exhibits non-local attribute near the crack tip and the maximum stress is in agreement with the non-local elasticity solution. Based on the local stress distribution, the fracture properties such as stress intensity factor and fracture toughness can be deduced directly from the maximum stress hypotheses. It is revealed that the stress intensity factors obtained from continuum models and discrete models are close to each other; therefore it can be used to predict the state of stress field near the crack tip for both continuum solids and atomistic structures. On the other hand, in the discrete models, the fracture toughness is found to be sensitive to the crack length

when the length is below 40 lattices. The smaller the crack length is, the lower the fracture toughness will be. Therefore, for the small crack length, the concept of LEFM may not be applicable to characterize the fracture behaviors of atomistic graphene structure.

Reference

[1]   M. P. Allen, *Computer Simulation of Liquids*. Oxford: Oxford University Press, 1987.

[2]   K. S. Cheung and S. Yip, "Atomic level stress in an inhomogeneous system," *Journal of Applied Physics,* vol. 70, p. 5688, 1991.

[3]   D. H. Tsai, "The virial theorem and stress calculation in molecular dynamics," *The Journal of Chemical Physics,* vol. 70, p. 1375, 1979.

[4]   J. Cormier, J. M. Rickman, and T. J. Delph, "Stress calculation in atomistic simulations of perfect and imperfect solids," *Journal of Applied Physics,* vol. 89, p. 99, 2001.

[5]   Z. S. Basinski, M. S. Duesbery, and R. Taylor, "Influence of shear stress on screw dislocations in a model sodium lattice," *Canadian Journal of Physics,* vol. 49, p. 2160, 1971.

[6]   R. J. Hardy, "Formulas for determining local properties in molecular dynamics simulations: Shock waves," *The Journal of Chemical Physics,* vol. 76, p. 622, 1982.

[7]   Z. H. Sun, X. X. Wang, A. K. Soh, and H. A. Wu, "On stress calculations in atomistic simulations," *Modelling and simulation in materials science and engineering,* vol. 14, p. 423, 2006.

[8]   J. A. Zimmerman, E. B. Webb, J. J. Hoyt, R. E. Jones, P. A. Klein, and D. J. Bammann, "Calculation of stress in atomistic simulation," *Modelling and simulation in materials science and engineering,* vol. 12, p. 319, 2004.

[9]   E. B. Webb, J. A. Zimmerman, and S. C. Seel, "Reconsideration of continuum thermomechanical quantities in atomic scale simulations," *Mathematics and Mechanics of Solids,* vol. 13, p. 221, 2008.

[10]   A. Hashimoto, K. Suenaga, A. Gloter, K. Urita, and S. Iijima, "Direct evidence for atomic defects in graphene layers," *Nature,* vol. 430, p. 870, 2004.

[11] J. C. Meyer, C. Kisielowski, R. Erni, M. D. Rossell, M. F. Crommie, and A. Zettl, "Direct imaging of lattice atoms and topological defects in graphene membranes," *Nano Letters,* vol. 8, p. 3582, 2008.

[12] J. L. Tsai, S. H. Tzeng, and Y. J. Tzou, "Characterizing the fracture parameters of a graphene sheet using atomistic simulation and continuum mechanics," *International Journal of Solids and Structures,* vol. 47, p. 503, 2009.

[13] Y. Jin and F. G. Yuan, "Nanoscopic Modeling of Fracture of 2D Graphene Systems," *Journal of Nanoscience and Nanotechnology,* vol. 5, p. 601, 2005.

[14] J. Cho, J. J. Luo, and I. M. Daniel, "Mechanical characterization of graphite/epoxy nanocomposites by multi-scale analysis," *Composites Science and Technology,* vol. 67, p. 2399, 2007.

[15] A. K. Rappe and C. J. Casewit, *Molecular Mechanics Across Chemistry*. California: University Science Books, 1997.

[16] C. Li and T. W. Chou, "Elastic moduli of multi-walled carbon nanotubes and the effect of van der Waals forces," *Composites Science and Technology,* vol. 63, p. 1517, 2003.

[17] W. D. Cornell, P. Cieplak, C. I. Bayly, I. R. Gould, K. M. Merz, D. M. Ferguson, D. C. Spellmeyer, T. Fox, J. W. Caldwell, and P. A. Kollman, "A second generation force field for the simulation of proteins, nucleic acids, and organic molecules," *Journal of the American Chemical Society,* vol. 117, p. 5179, 1995.

[18] Ulrich Burkert and N. L. Allinger, *Molecualr Mechanics*. Washington: American Chemical Society, 1982.

[19] B. Holian, "Hoover NPT dynamics for systems varying in shape and size," *Molecular Physics,* vol. 78, p. 533, 1993.

[20] W. Smith and T. R. Forester, *The DL_POLY User Manual, version 2.13*. England: Daresbury Laboratory, 2001.

[21]   J. F. Lutsko, "Stress and elastic constants in anisotropic solids: Molecular dynamics techniques," *Journal of Applied Physics,* vol. 64, p. 1152, 1988.

[22]   S. Iijima, P. M. Ajayan, and T. Ichihashi, "Growth model for carbon nanotubes," *Physical review letters,* vol. 69, p. 3100, 1992.

[23]   T. L. Anderson, *Fracture Mechanics: Fundamentals and Applications*. Boca Raton: CRC Press, 1995.

[24]   A. C. Eringen, C. G. Speziale, and B. S. Kim, "Crack tip problem in non-local elasticity," *Journal of Mechanics and Physics of Solids,* vol. 25, p. 339, 1977.

[25]   I. N. Sneddon, *Fourier Transforms*. New York: McGraw-Hill, 1951.

[26]   I. S. Gradshteyn and I. M. Ryzhik, *Table of Integral, Series and Products*. New York: Academic Press, 1980.

[27]   Z. Zhou and B. Wang, "Investigation of a griffith crack subject to uniform tension using non-local theory by a new method," *Applied Mathematics and Mechanics,* vol. 20, p. 1099, 1999.

[28]   A. Adnan and C. T. Sun, "Evolution of nanoscale defects to planar cracks in a brittle solid," *Journal of the Mechanics and Physics of Solids,* vol. 58, p. 983, 2010.

Appendix A

MATLAB code of calculating non-local stress field for crack-tip problem using Gaussian function as distribution curve

```
%--------beginning of the code-----------------------
clc;
clear;
%--------Eringen's non-local elasticity----------------
% Reference:
% Eringen, A.C., Speziale, C.G., Kim, B.S., 1977.
% Crack-tip problem in non-local elasticity. Journal of the Mechanics and
Physics of Solids 25, 339¡V355.
% Distribution curve alpha is Gaussian function
%----------input parameters--------------------------------
ad=2.46;                   % graphene lattice length
L=2.46*23/2;               % half crack length (L)
h=1.9;                     % smoothing length in Gaussian function
beta=ad/h;
e=ad/(2*beta);
tou=-2;                    % applied loading on "crack surface" unit: GPa
ndiv=1000;                 % output data number
tol=1e-10;                 % integral error tolerance
x=linspace(0.0*L,2.0*L,ndiv); % interval of stress field


%-------------calculating non-local stress field-----------------
for i=1:ndiv
    xx=x(i)/L;


f=@(K)besselj(1,K).*cos(K*xx).*((1-erf(e*K/L)).*(1-2*(e*K/L).^2)+(2*(
e*K/L)/sqrt(pi)).*exp(-(e*K/L).^2));    % eqn. (4.1.52) in the thesis


y(i)=quadgk(f,0,inf,'RelTol',tol,'AbsTol',tol,'MaxIntervalCount',8000
);
end


%-----------superposition of stress field---------------------
str=tou*y-tou;
xx=(x'-L)./ad;        % plot data from crack tip and normalized the position
                      % with respect to lattice
```

```
str=str'./(-tou);              % normalized the stress field with respect
                                % to applied loading
plot(xx,str,'r')


%------------end of the code--------------------------------
```

Appendix B

MATLAB code of calculating non-local stress field for crack-tip problem using Triangular function as distribution curve

```
%--------beginning of the code-----------------------
clc;
clear;
%--------Eringen's non-local elasticity----------------
% Reference:
% Eringen, A.C., Speziale, C.G., Kim, B.S., 1977.
% Crack-tip problem in non-local elasticity. Journal of the Mechanics and
Physics of Solids 25, 339;V355.
% Distribution curve alpha is Triangular function


%----------input parameters---------------------------------
ad=2.46;                    % graphene lattice length
L=2.46*23/2;                % half crack length (L)
e=ad/L;
ndiv=3000;                  % output data number
tol=1e-10;                  % integral error tolerance
uplim=2*pi*L/ad;            % upper limit of integral, as suggested in
                            %Eringen's paper
x=linspace(0.0*L,2*L,ndiv); % interval of stress field
p=2;                        % applied loading on "crack surface" unit: GPa


%-------------calculating non-local stress field-----------------
xx=x./L;
% the following is the eqn. (4.1.57) in the thesis
f=@(K)(-6/pi*((13/30*(K*e).^-1+32/15*(K*e).^-3-1/20*(K*e)).*cos((K*e)
)+(19/30*(K*e).^-2-1/20).*sin((K*e))+(1/3-1/20*(K*e).^2).*sinint(K*e)
-1/6*pi-32/15*(K*e).^-3+pi/40*(K*e).^2)).*besselj(1,K).*cos(K.*xx).*(
-p);
y=quadv(f,0,uplim);


%-----------superposition of stress field----------------------
yy=y+p;
yy=yy./p;                   % normalized the stress field with respect
                            % to applied loading
xx=x-L;                     % plot data from crack tip and normalized the
```

53

```
                              %position with respect to lattice
xx=xx'./ad;

plot(xx,yy,'b')


%------------end of the code-------------------------------
```

Table 3.1.1 Cut-off radius corresponding to different smoothing lengths h

	h=1.8	h=2.5	h=3.0
R_c (Å)	8	9	12

Table 4.2.1 Dimension of finite element model with different crack lengths

Unit: Å	2L/a=3	2L/a=41	2L/a=81
2W	73.8	1008.6	1992.6
2H	76.68	1005.36	1985.16
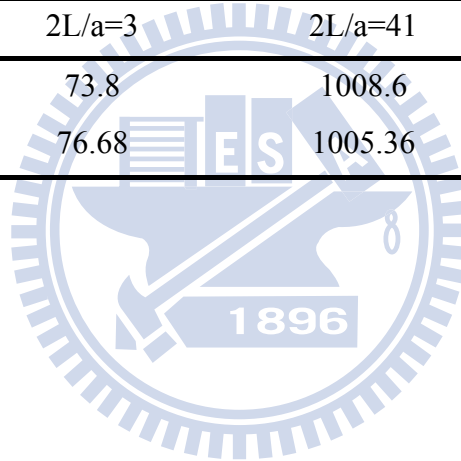
Table 4.2.2 Material properties of graphene sheet obtained from MD simulation

Young's Modulus (GPa)	Poisson's ratio
790.7	0.27

Table 4.3.1 Different widths of discrete graphene model with crack length of 5 lattices

Unit: Å	L/W=0.05	L/W=0.1	L/W=0.3
2W	246	123	49.2
2H	247.08	119.28	51.12
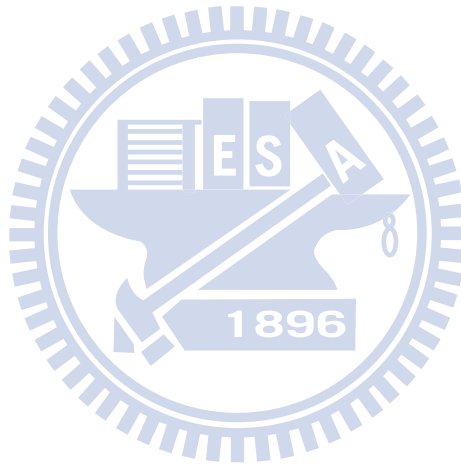
Table 4.3.2 Dimension of discrete graphene model with different crack lengths

	2L/a								
	3	5	7	19	21	23	41	61	81
2W	73.8	123	172.2	467.4	516.6	565.8	1008.6	1500.6	1992.6
2H	76.68	119.28	170.4	468.6	519.72	562.32	1005.36	1499.52	1985.16

Unit: Å

Table 4.3.3 Maximum local stress with different crack lengths

2L/a	Maximum stress (GPa)		
	Non-local (Gaussian function)	Hardy stress	Tsai stress
3	2.705	2.588	3.29
5	3.224	3.171	4.19
7	3.678	3.672	4.94
19	5.701	5.850	8.08
21	5.967	6.141	8.49
23	6.230	6.412	8.88
41	8.198	8.503	11.84
61	9.950	10.356	14.44
81	11.431	11.923	16.64
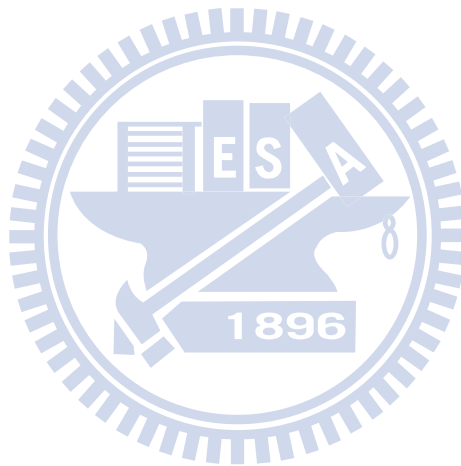
Table 4.4.1 Stress intensity factor from Hardy, FEM and continuum mechanics

2L/a	K_I ($Pa\sqrt{m}$)x10^4			
	Hardy stress	FEM	$K_I = \sigma_0 \sqrt{\pi L}$	Error (Hardy with FEM)
3	6.44	6.99	6.81	-7.87 %
5	8.26	8.92	8.79	-7.40 %
7	9.67	10.39	10.40	-6.93 %
19	16.12	17.02	17.14	-5.29 %
21	17.02	17.88	18.02	-4.81 %
23	17.87	18.70	18.85	-4.44 %
41	24.23	25.26	25.17	-4.08 %
61	29.34	30.42	30.71	-3.55 %
81	34.04	35.28	35.38	-3.51 %

Table 4.4.2 Stress concentration factor with different crack lengths

2L/a	C	
	Non-local (Gaussian function)	Hardy stress
3	0.781	0.747
5	0.721	0.709
7	0.695	0.694
19	0.654	0.671
21	0.651	0.670
23	0.649	0.669
41	0.640	0.664
61	0.637	0.663
81	0.635	0.662
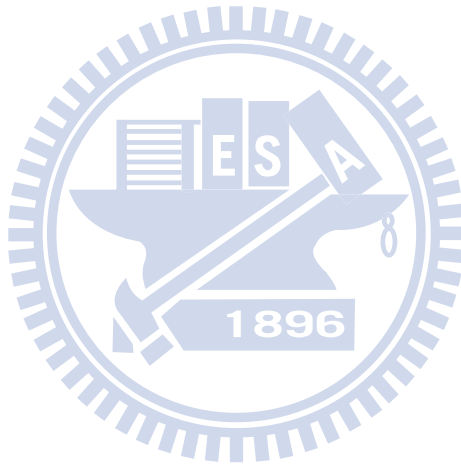
Table 4.4.3 Applied loading to achieve σ_c with different crack lengths

2L/a	σ_0 (GPa)	
	Non-local (Gaussian function)	Hardy stress
3	0.739	0.773
5	0.620	0.631
7	0.544	0.545
19	0.351	0.342
21	0.335	0.326
23	0.321	0.312
41	0.244	0.235
61	0.201	0.193
81	0.175	0.168

Table 4.4.4 Fracture toughness with different crack lengths

2L/a	K_{IC} ($Pa\sqrt{m}$)x10^4	
	Non-local (Gaussian function)	Hardy stress
3	2.517	2.632
5	2.726	2.773
7	2.828	2.832
19	3.006	2.930
21	3.020	2.934
23	3.029	2.938
41	3.071	2.960
61	3.086	2.965
81	3.096	2.969
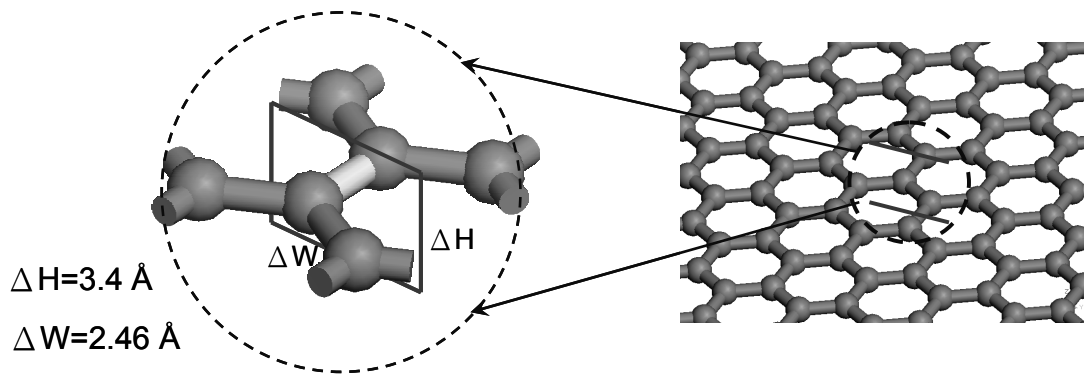
Fig. 3.1.1 Dimension of the dividing plane adopted in Tsai's stress formulation

ΔH=3.4 Å

ΔW=2.46 Å

$\lambda=1$ m $\lambda=0$

$$\mathbf{r}^{\alpha} - \mathbf{r} = \mathbf{r}^{m} \qquad \mathbf{r}^{\beta} - \mathbf{r} = \mathbf{r}^{1}$$
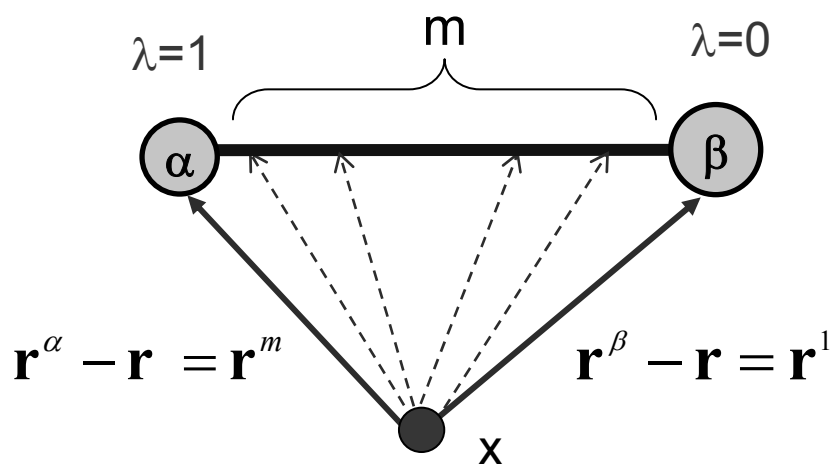
Figure 3.1.2 Interpretation of bond function
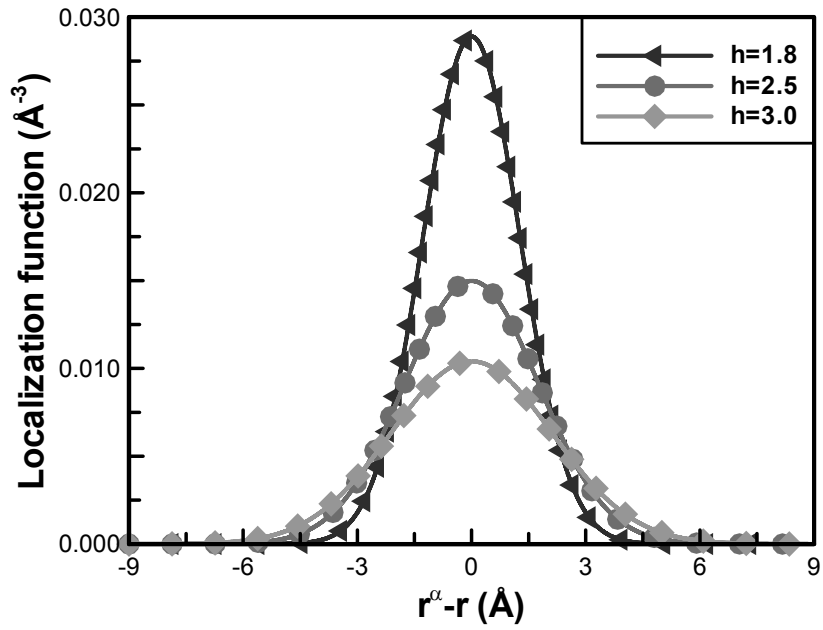
Figure 3.1.3 Localization functions with various smoothing lengths
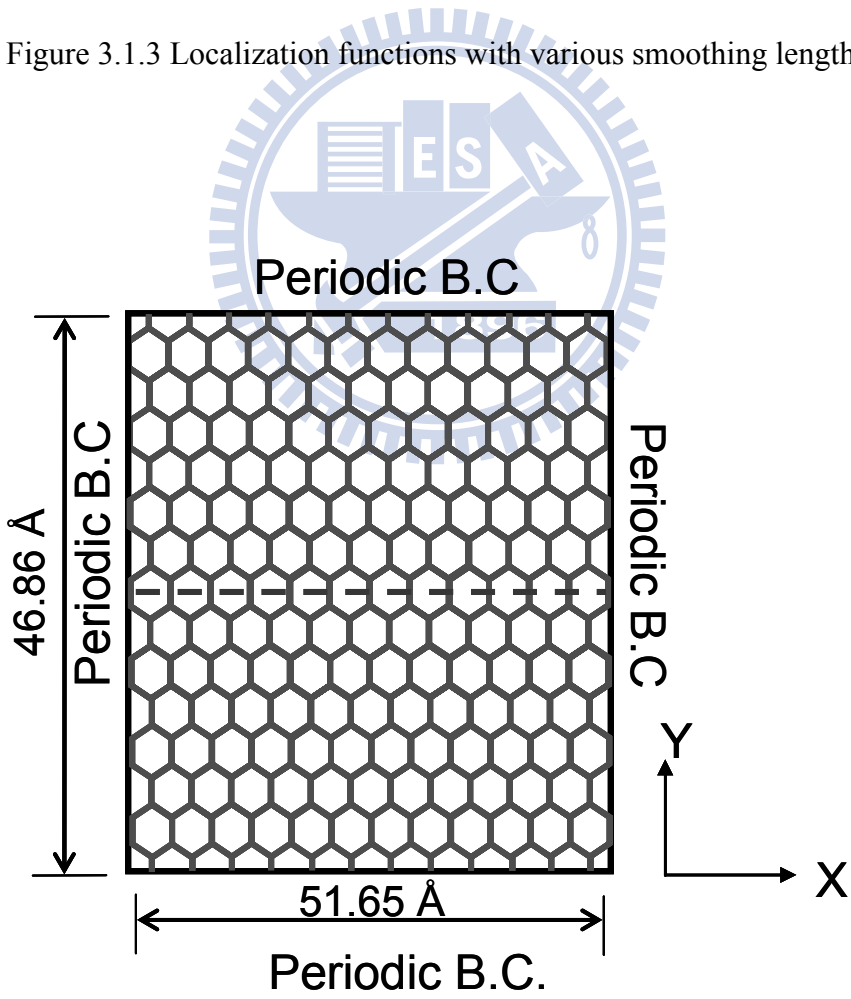
Figure 3.2.1 Continuous graphene sheet with periodic boundary conditions
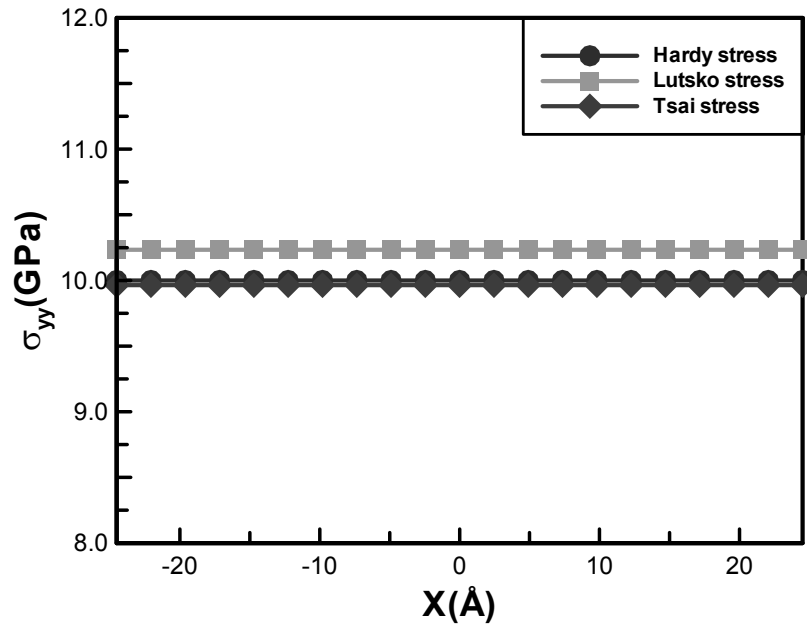
Figure 3.2.2 Local stress in the periodic graphene with bonded interaction
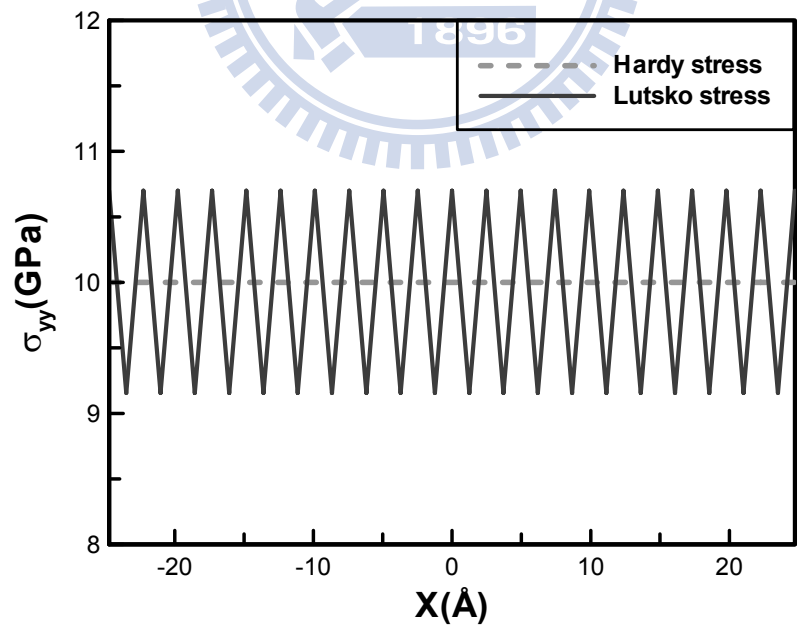
Figure 3.2.3 Hardy and Lutsko stress in the periodic graphene with bonded and
non-bonded interaction
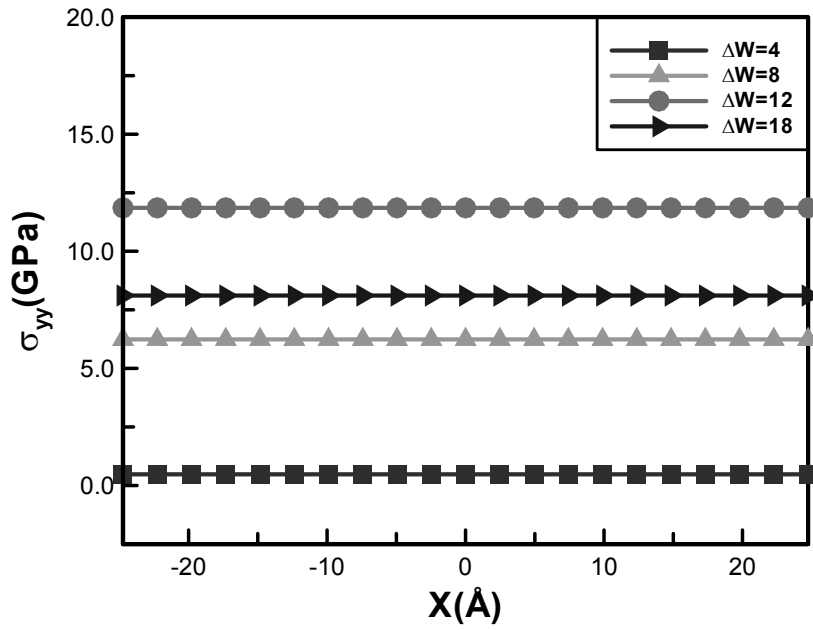
Figure 3.2.4. Tsai stress in the periodic graphene with bonded and non-bonded
interaction with different dividing planes
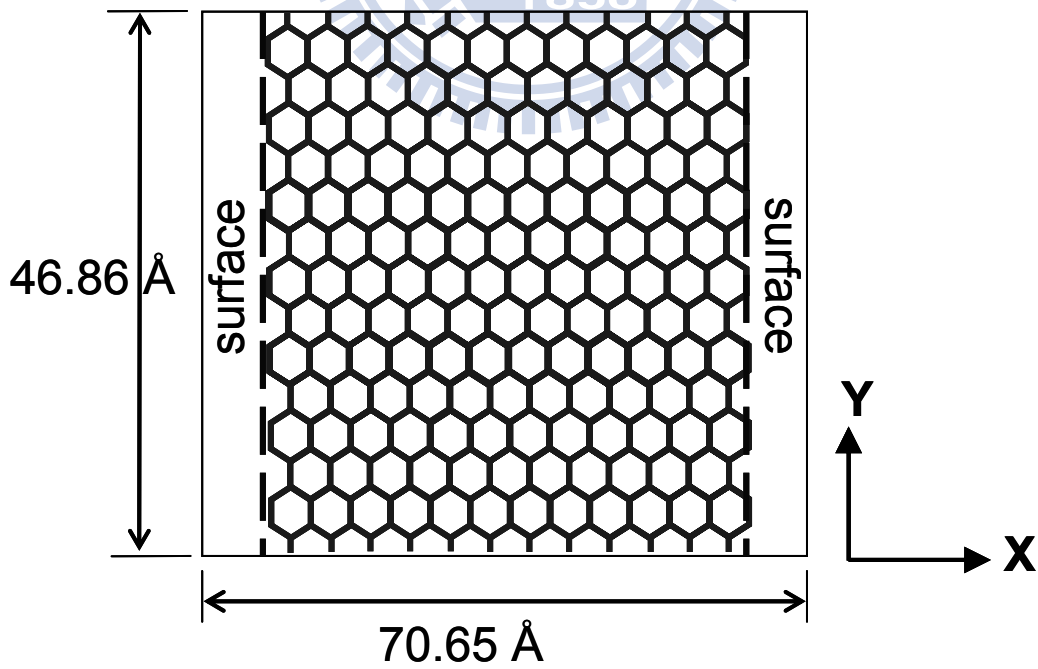
Figure 3.2.5 Finite graphene sheet with free surfaces in the x direction
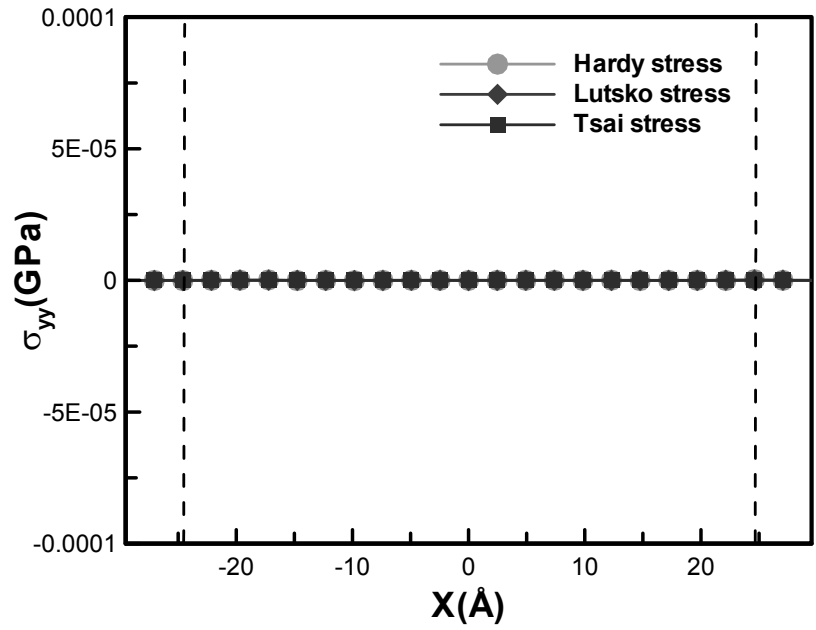
Figure 3.3.1 Local stress in the finite graphene sheet with bonded interaction
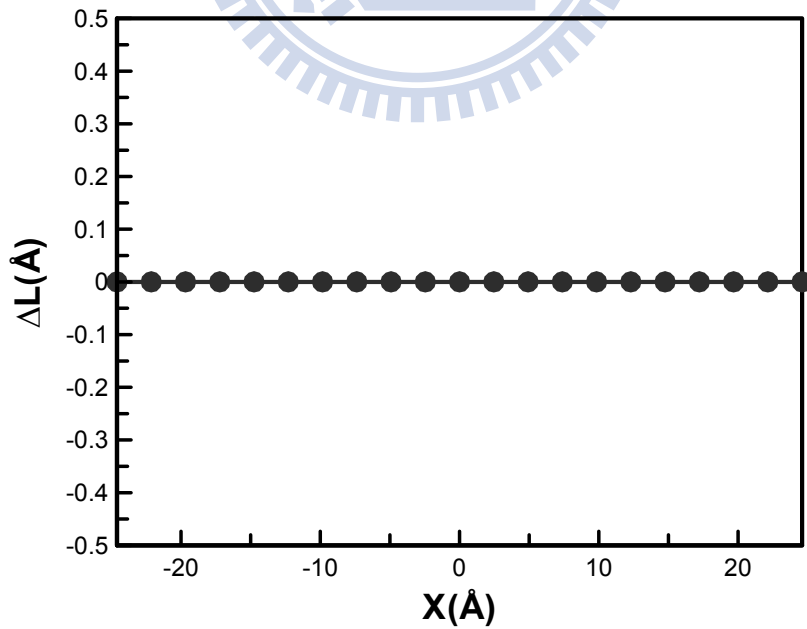
Figure 3.3.2 Bond length of finite graphene sheet with bonded interactions at stress free state

(a)

(b)
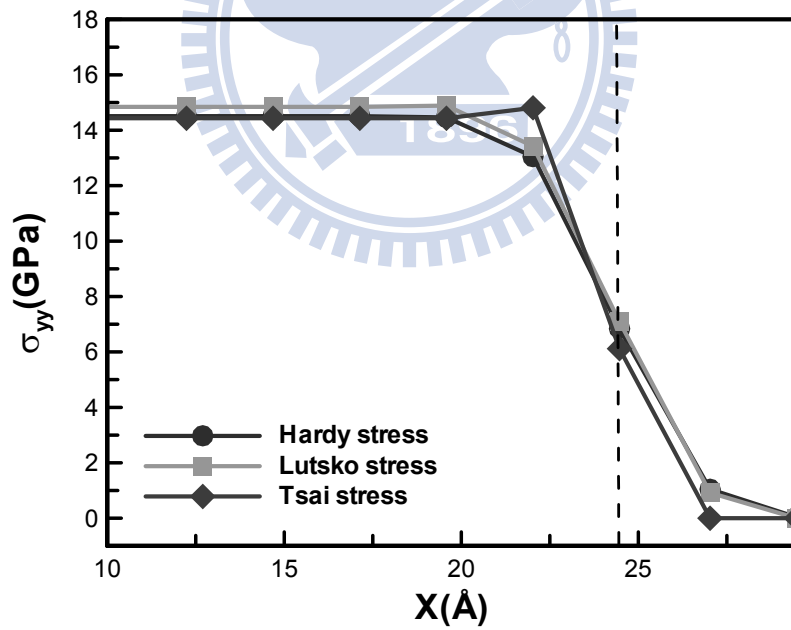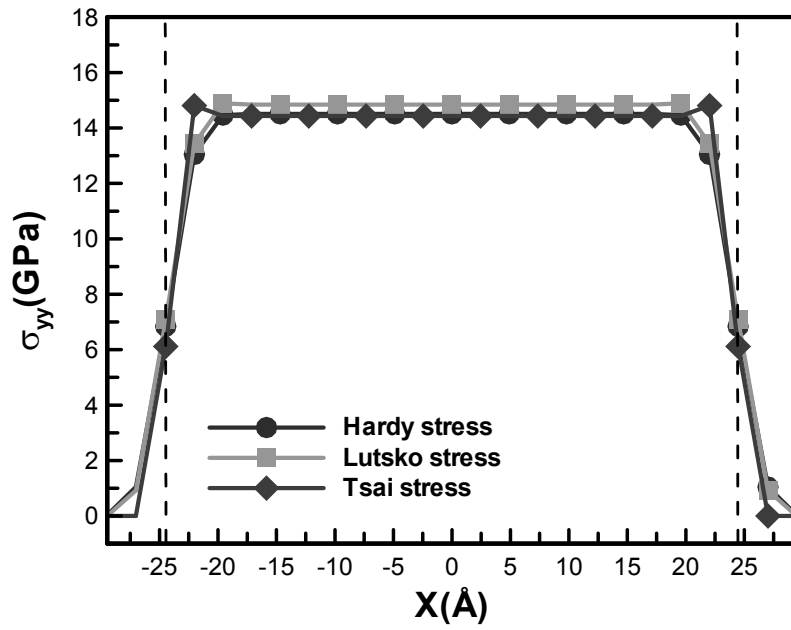
Figure 3.3.3 Local stress distribution in the finite graphene sheet with bonded
interactions (a) global view (b) local view
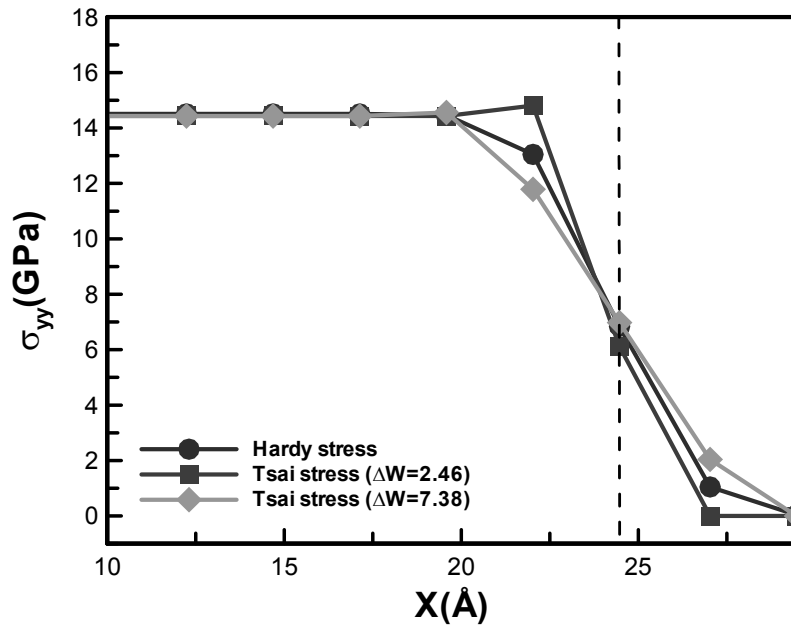
Figure 3.3.4 Tsai stress with different dividing planes in the finite graphene sheet with
bonded interactions near surface
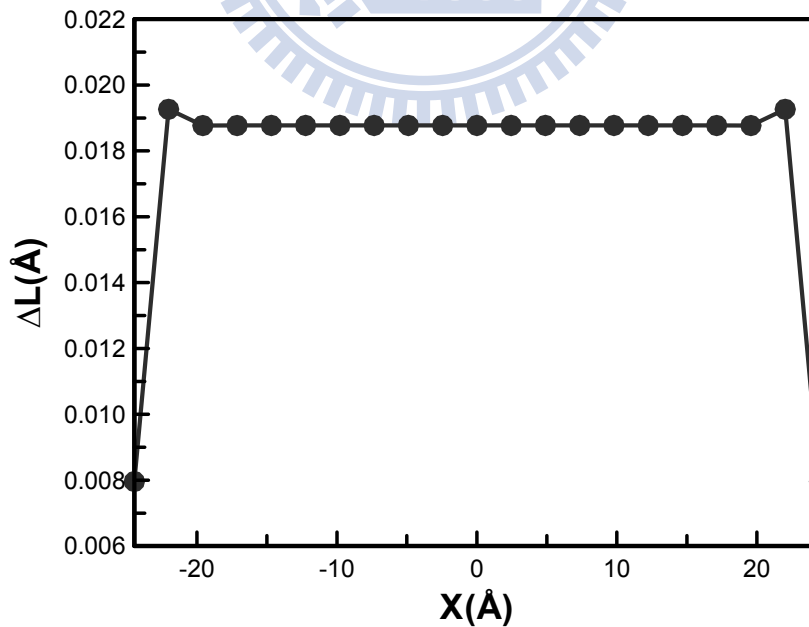
Figure 3.3.5 Bond length of the finite graphene sheet with bonded interactions at
uniaxial stress state
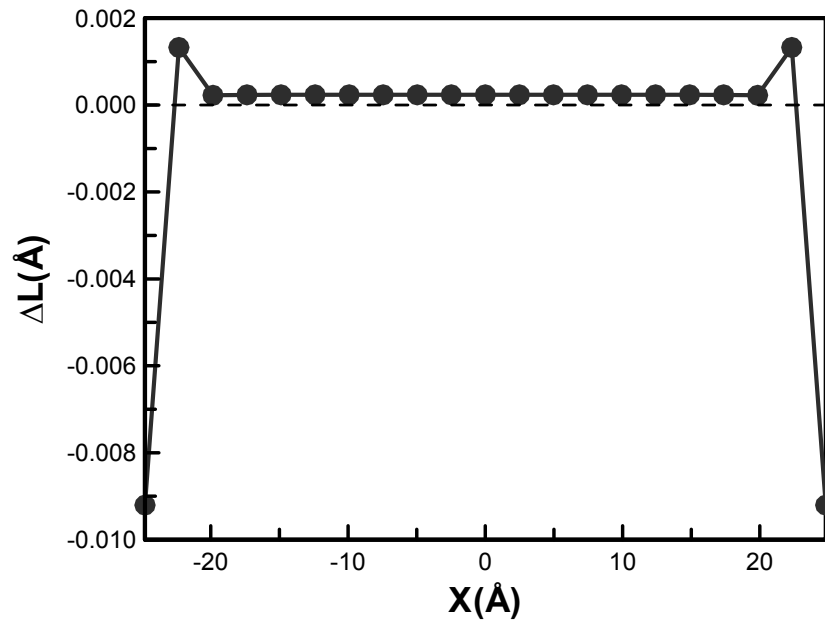
Figure 3.4.1 Variation of bond length for the finite graphene sheet with bonded and non-bonded interactions at stress free state
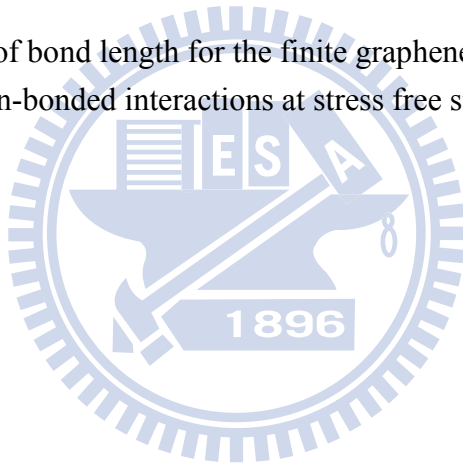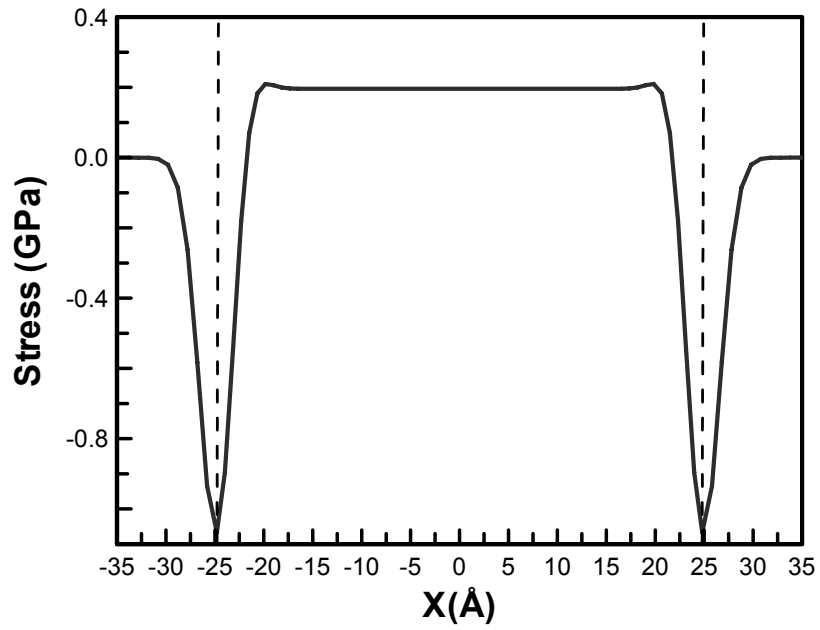
(a)
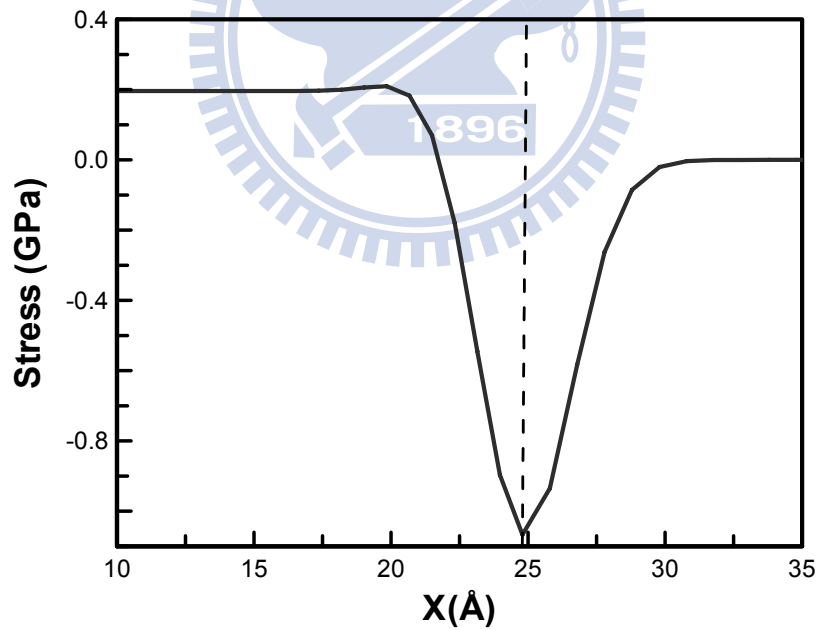
(b)

Figure 3.4.2 Hardy stress distribution of the finite graphene sheet with bonded and non-bonded interactions at stress free state (a) global view (b) local view
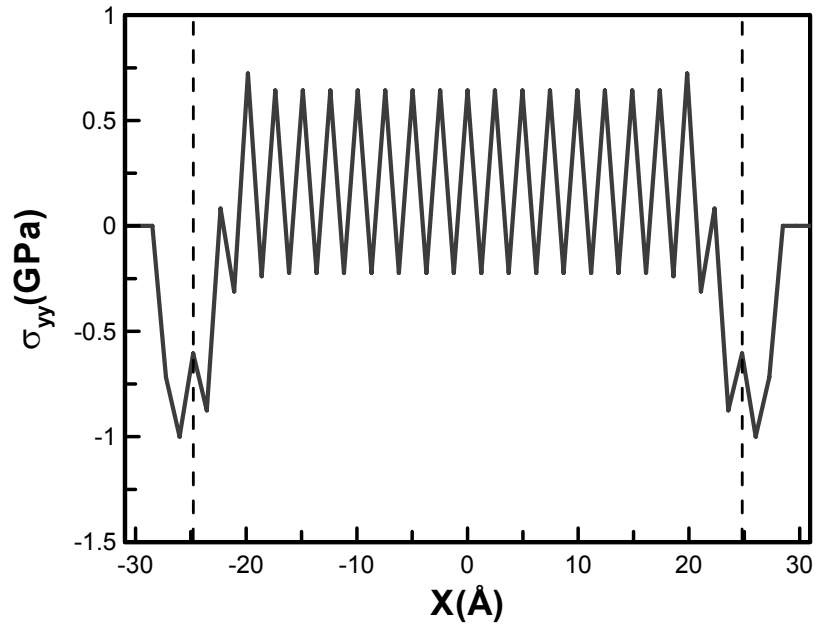
Figure 3.4.3 Lutsko stress distribution of the finite graphene sheet with bonded and non-bonded interactions at stress free state
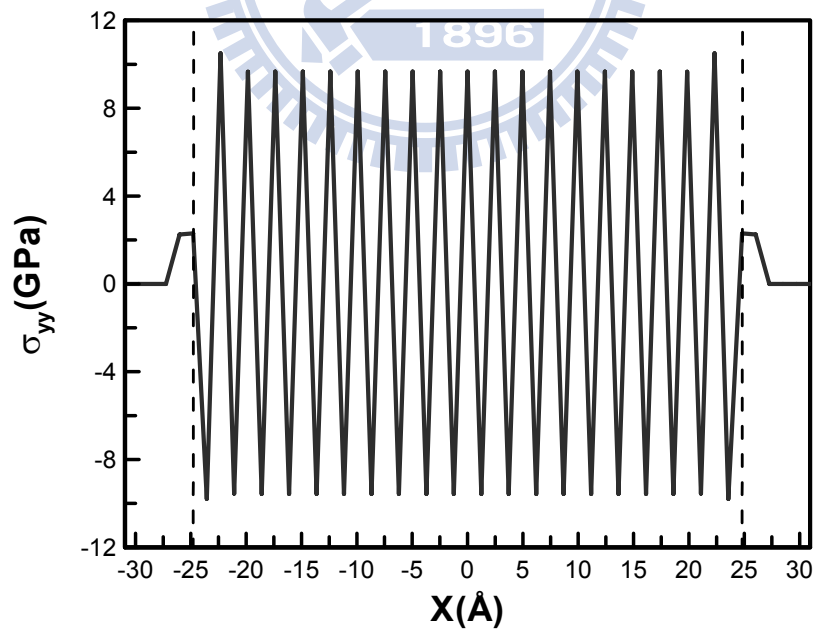
Figure 3.4.4 Tsai stress distribution of the finite graphene sheet with bonded and non-bonded interactions at stress free state
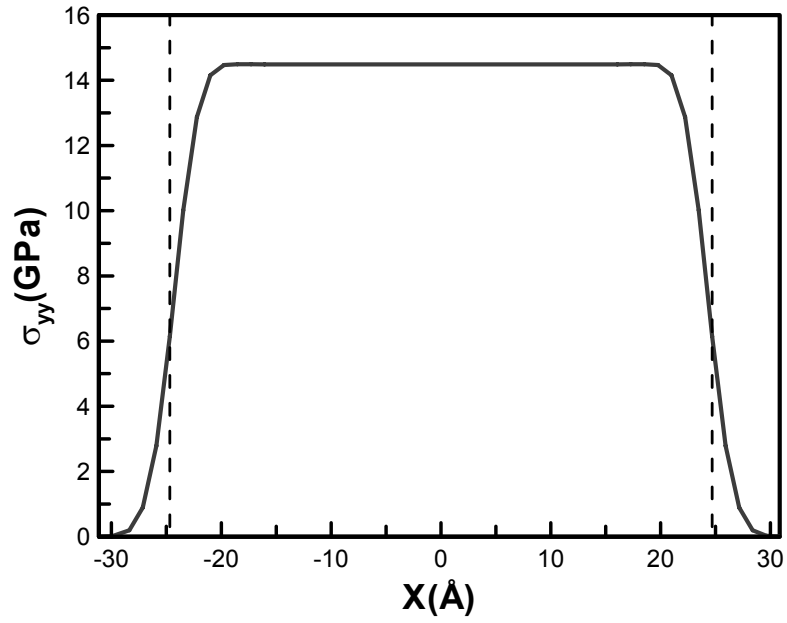
(a)
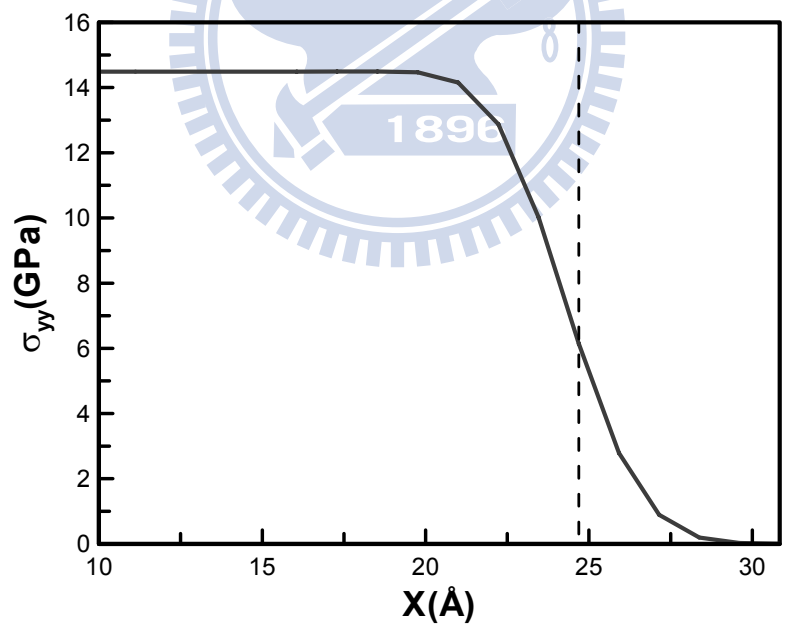
(b)

Figure 3.4.5 Hardy stress distribution of the finte graphene sheet with bonded and non-bonded interactions at uniaxial stress state (a) global view (b) local view
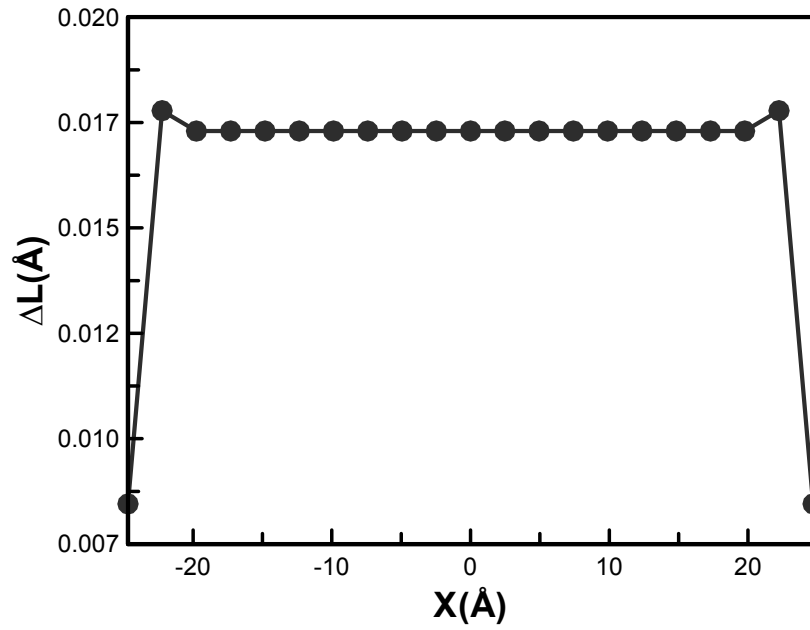
Figure 3.4.6 Variation of bond length for the finite graphene sheet with bonded
and non-bonded interactions at stress state of 10GPa
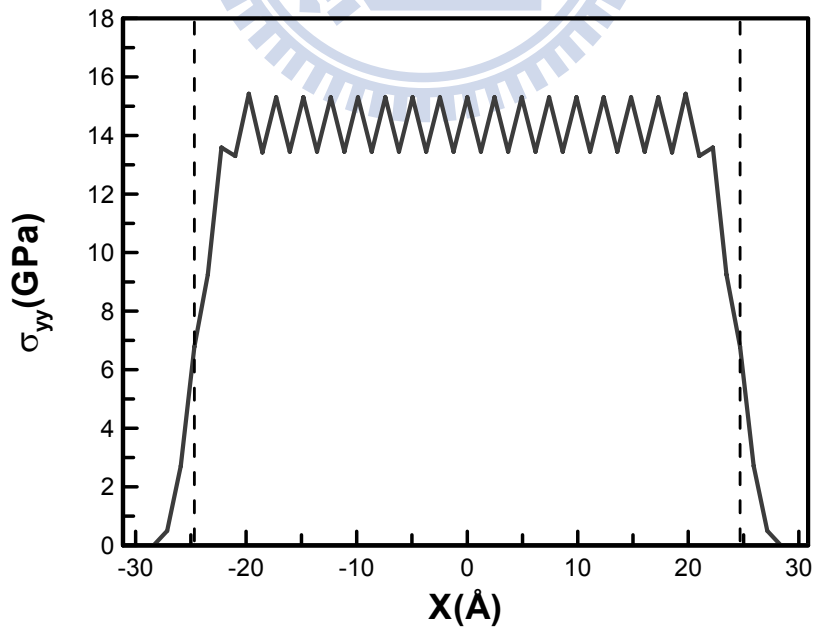
Figure 3.4.7 Lutsko stress distribution of the finite graphene sheet with bonded and
non-bonded interactions at uniaxial stress state
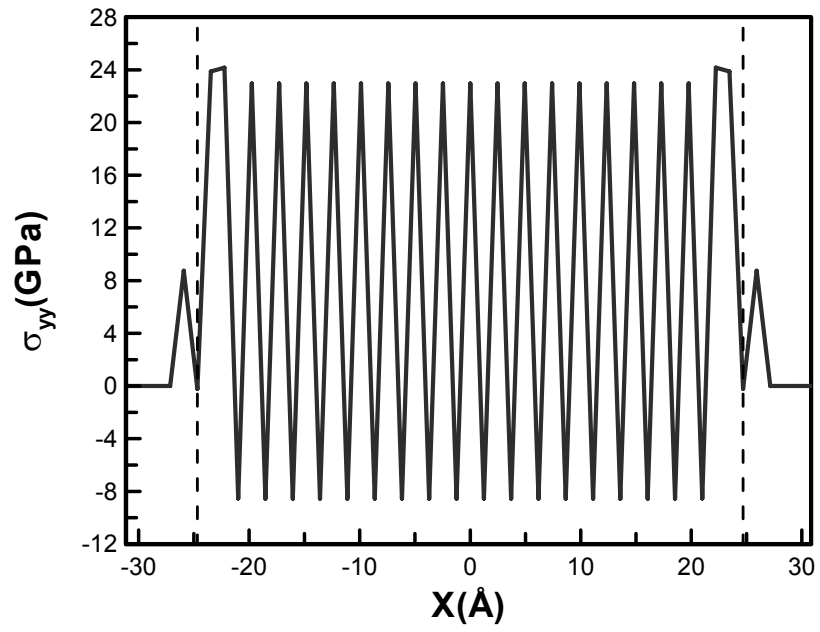
Figure 3.4.8 Tsai stress distribution of the finite graphene sheet with bonded and non-bonded interactions at uniaxial stress state
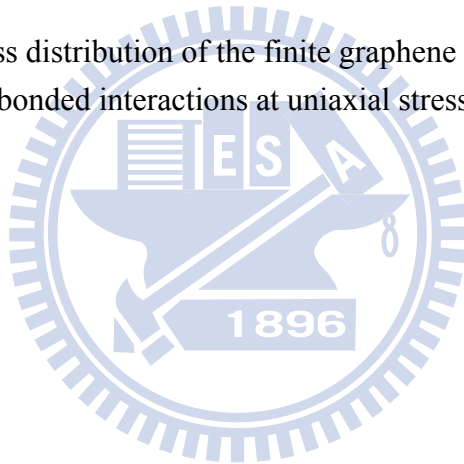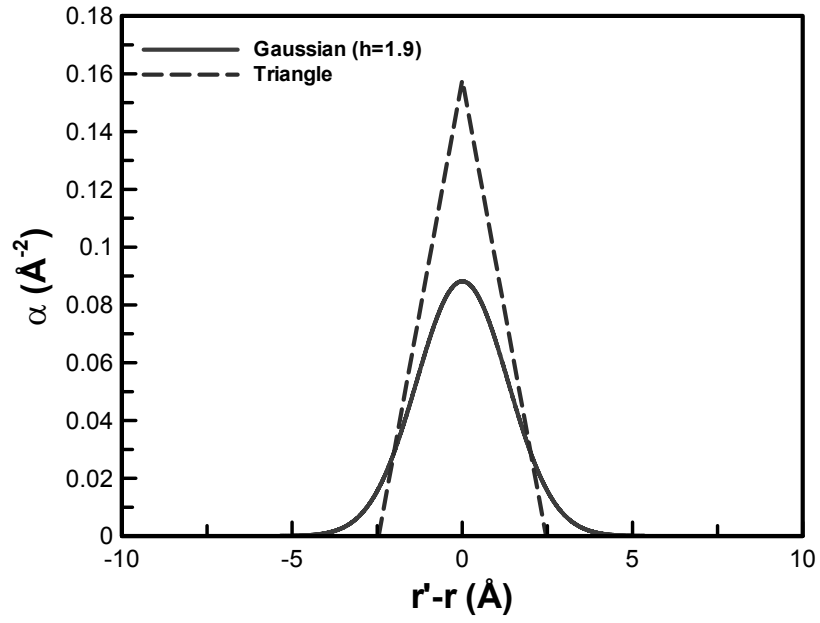
Fig. 4.1.1 Distribution curves α employed in non-local elasticity
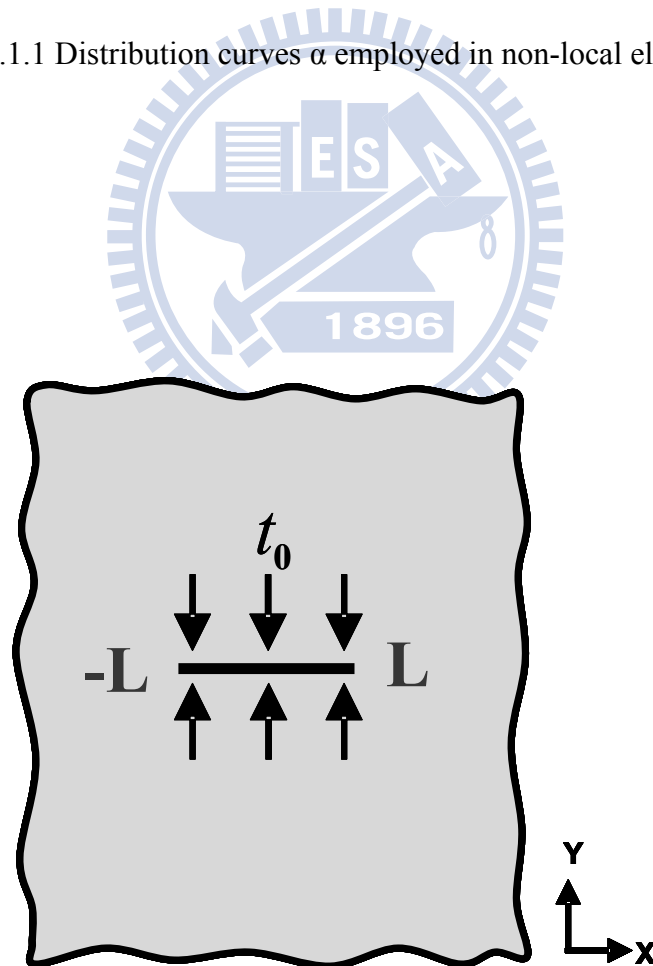
Fig. 4.1.2 Boundary conditions of the line-crack problem in non-local elasticity
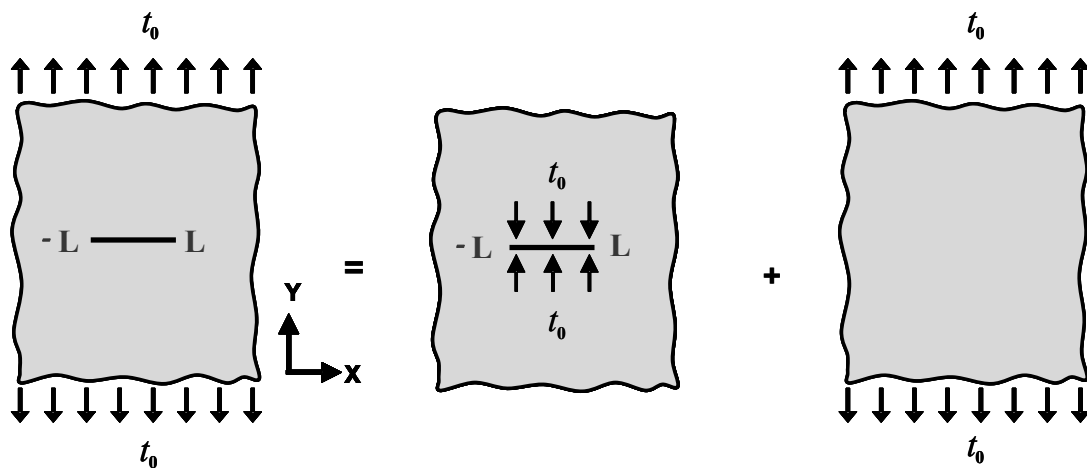
Fig. 4.1.3 Superimposition of the boundary condition in the non-local elasticity
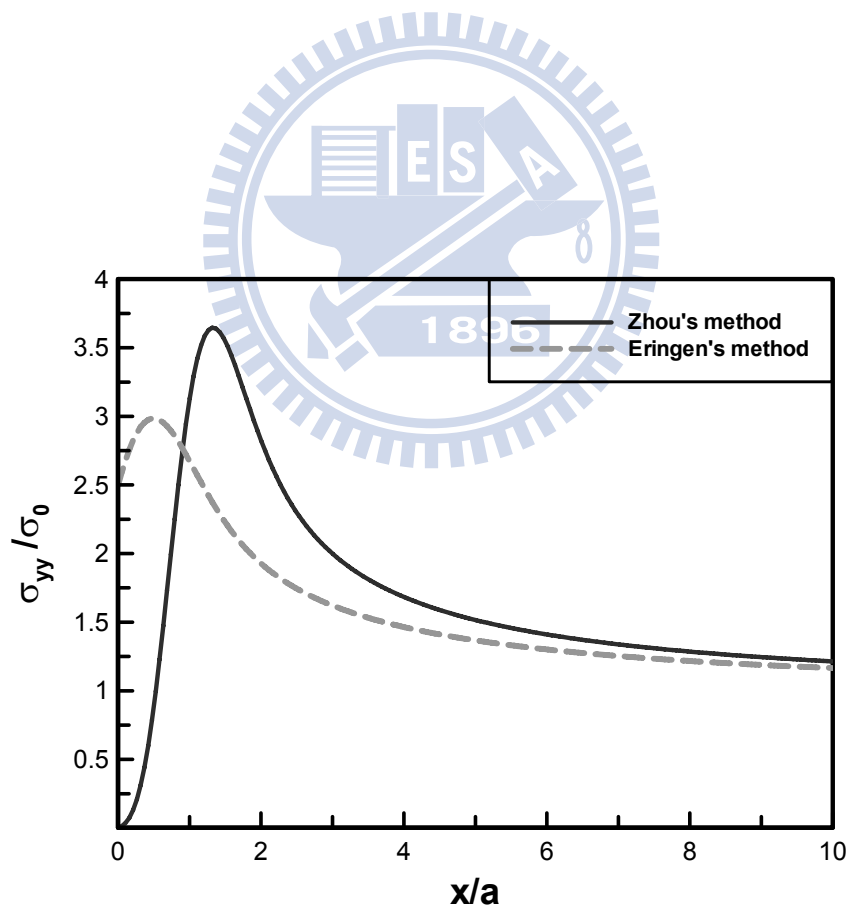
Fig. 4.1.4 Different methods of solving non-local elasticity problem
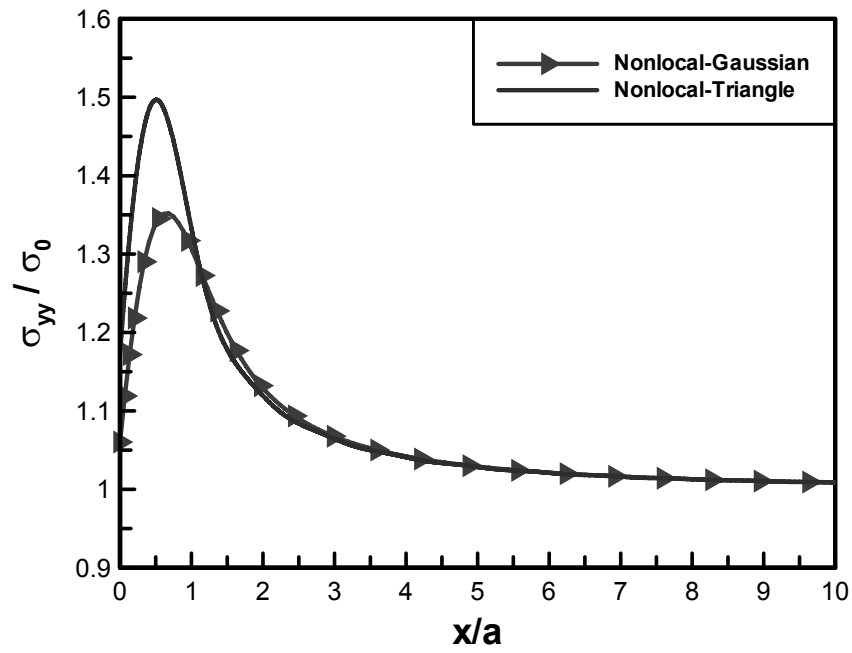
Fig. 4.1.5 Stress distribution in the graphene with crack lengths of 3 lattices
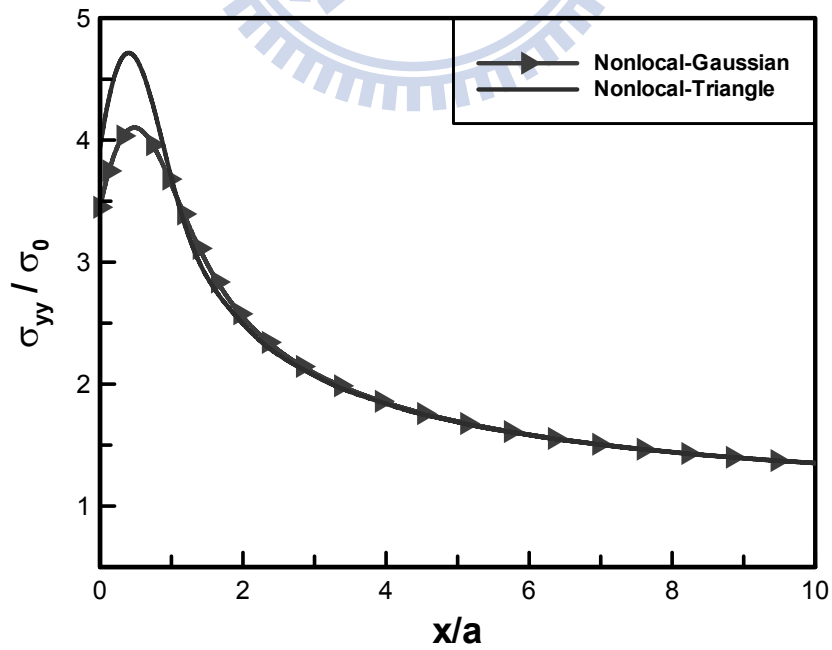
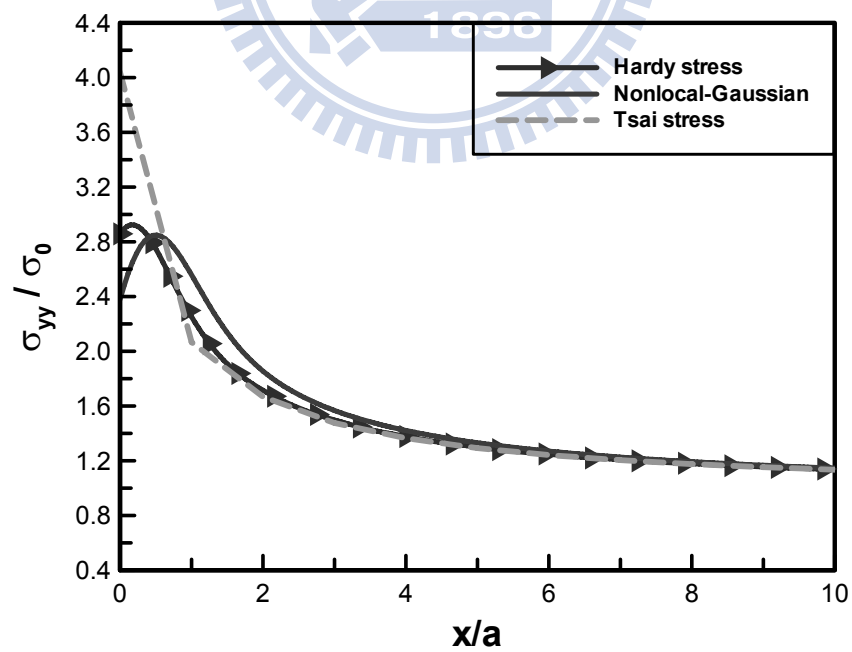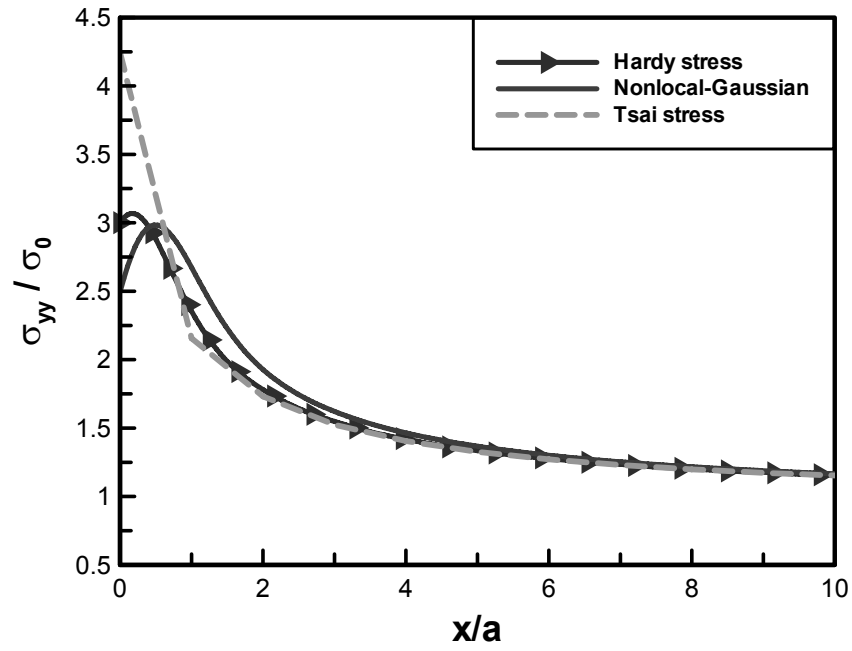Fig. 4.1.6 Stress distribution in the graphene with crack lengths of 41 lattices
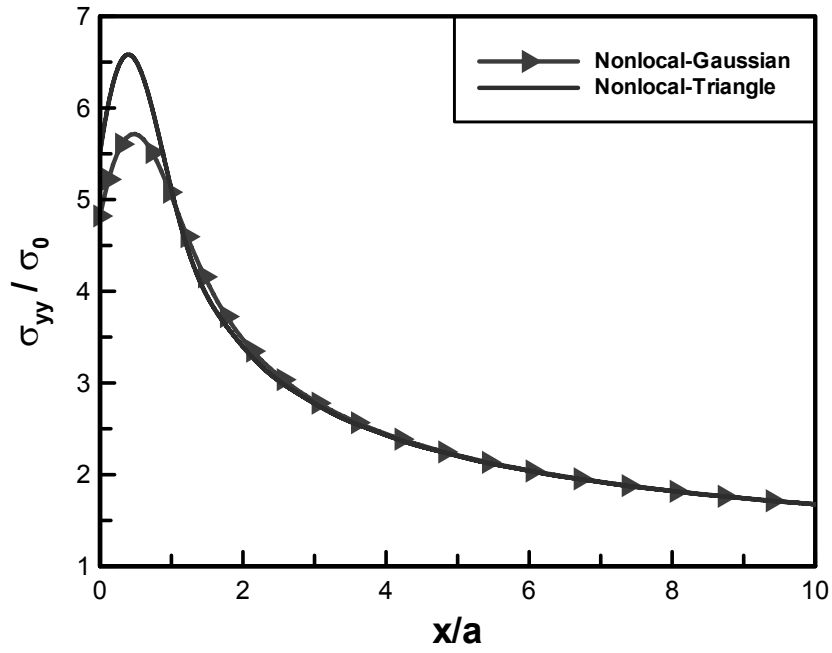
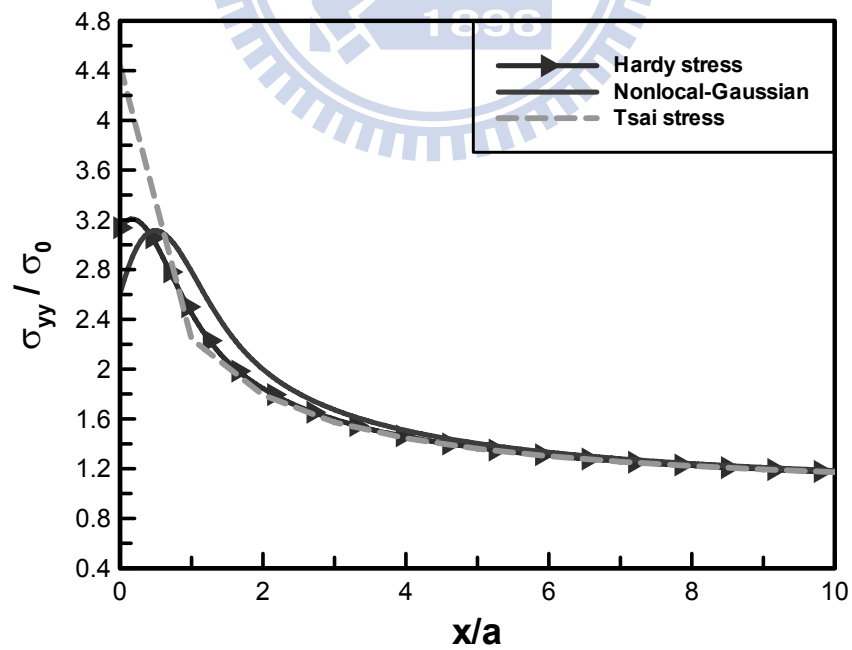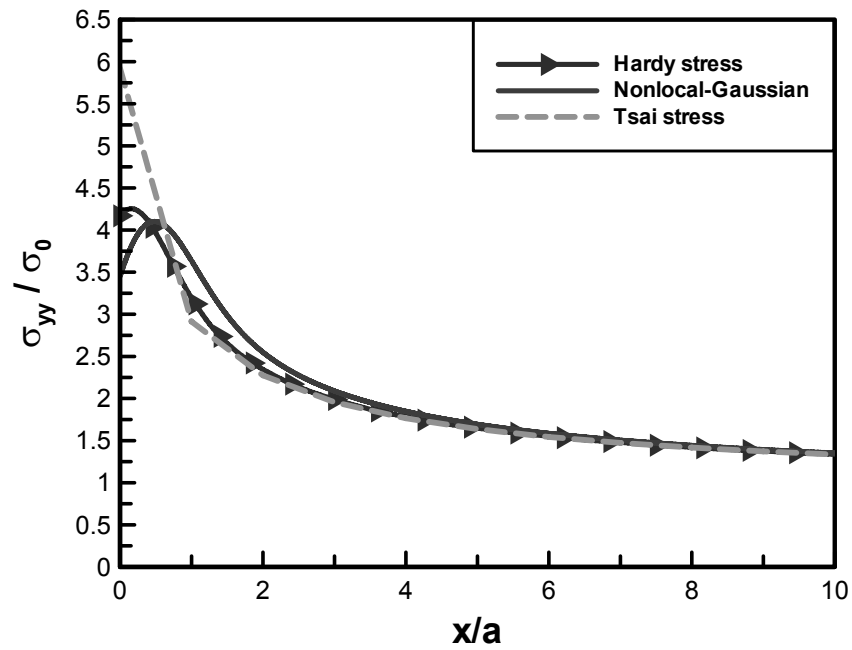Fig. 4.1.7 Stress distribution in the graphene with crack lengths of 81 lattices
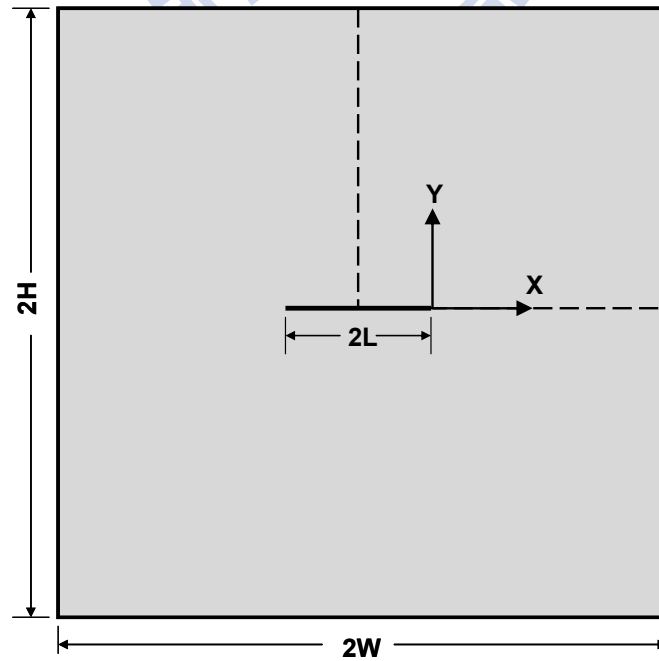
Fig. 4.2.1 Finite element model for continuum graphene sheet. Note that the dimension has different values for the three different models.
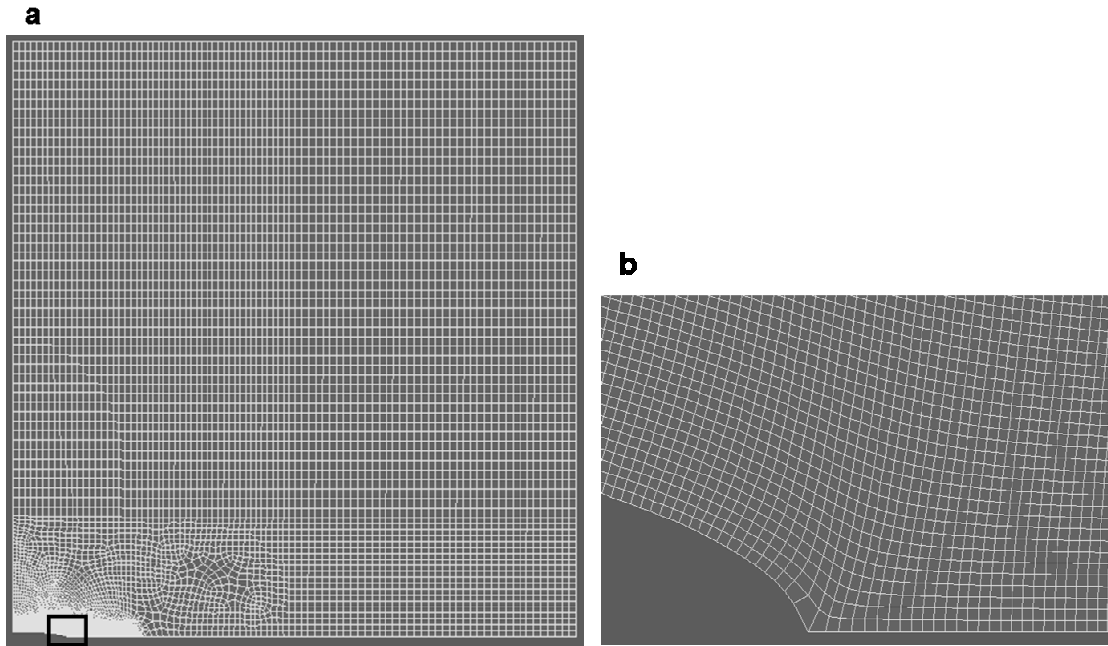
Fig. 4.2.2 Finite element mesh for the graphene with crack lengths of 41 lattices: (a) mesh for the entire model (quarter model) and (b) magnified view of the fine mesh around the crack tip.
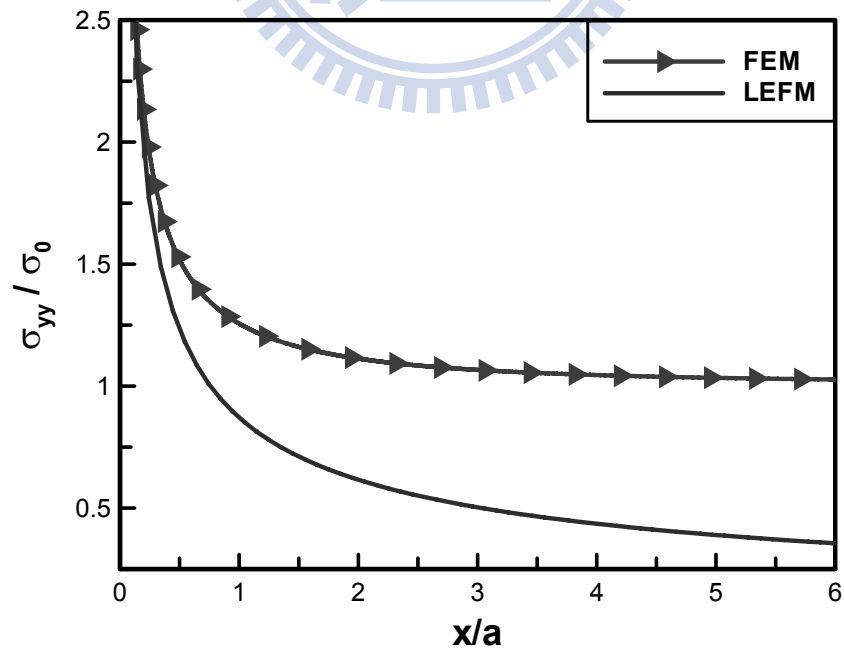
Fig. 4.2.3 Stress distribution in the graphene with crack lengths of 3 lattices
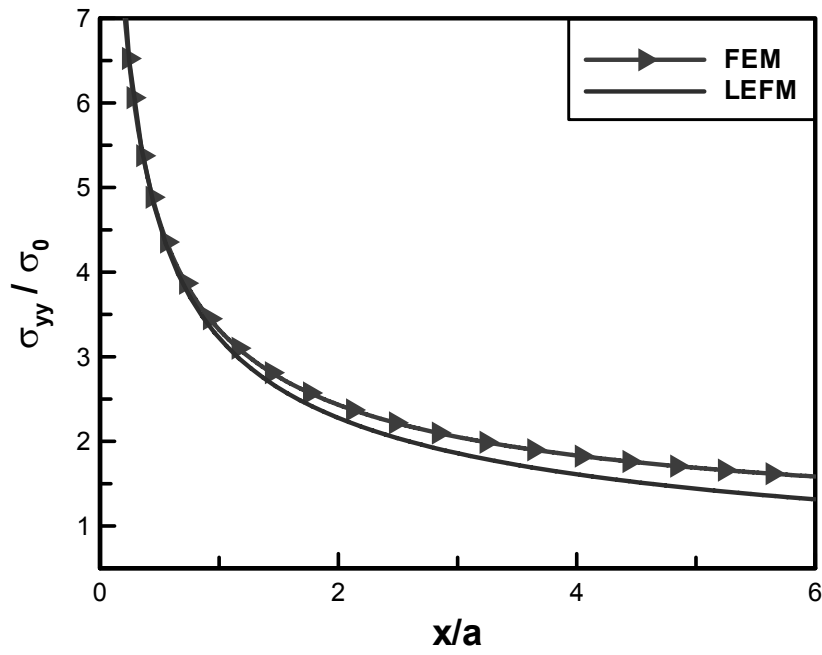
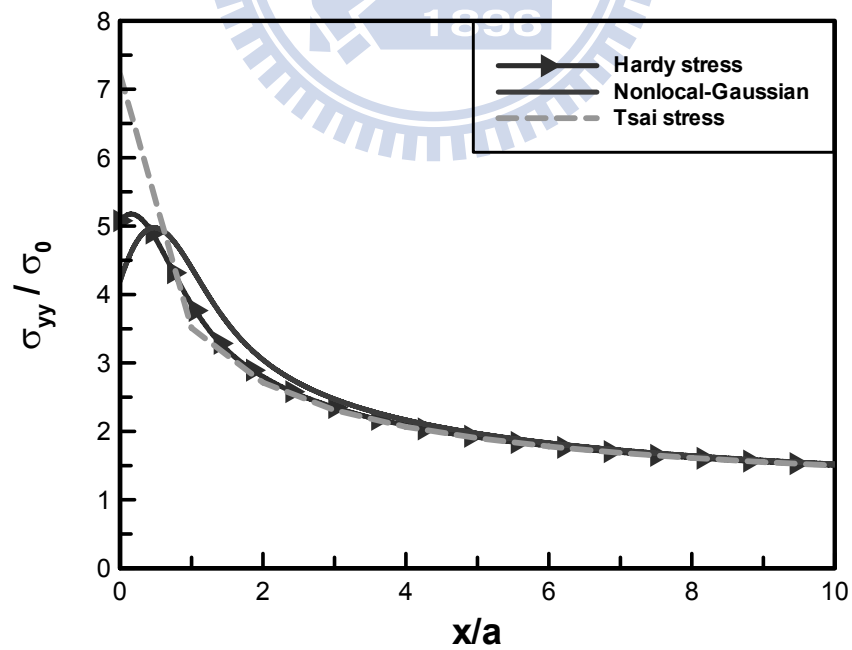Fig. 4.2.4 Stress distribution in the graphene with crack lengths of 41 lattices
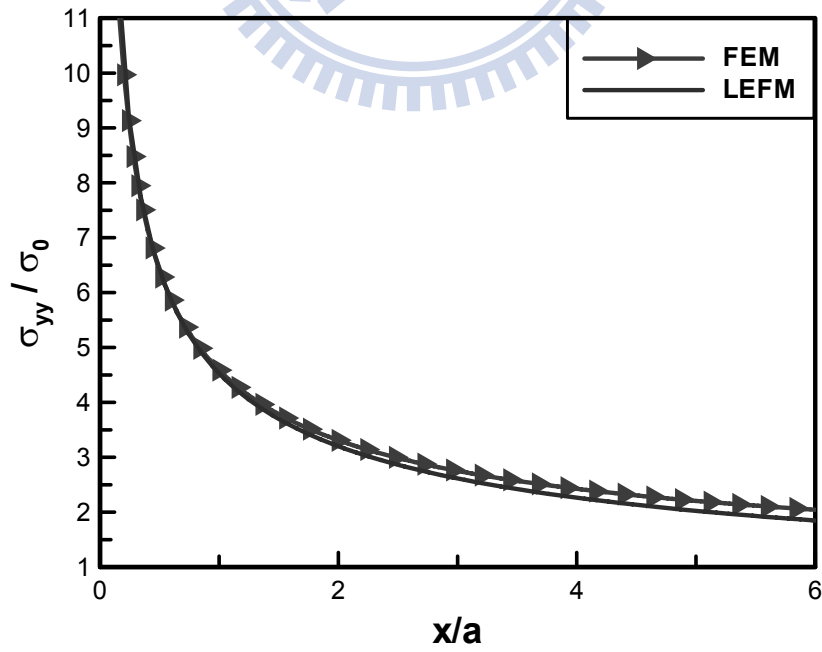
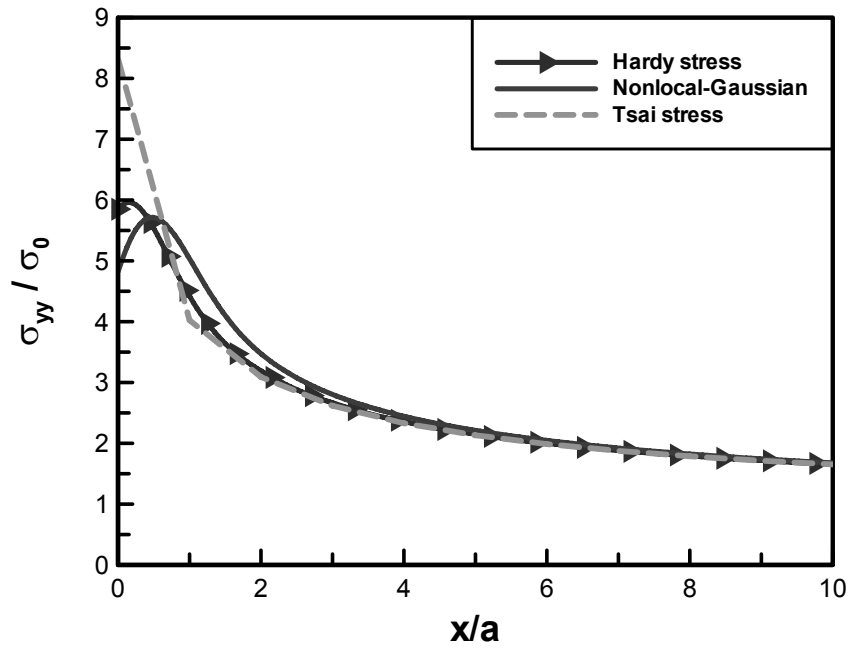Fig. 4.2.5 Stress distribution in the graphene with crack lengths of 81 lattices
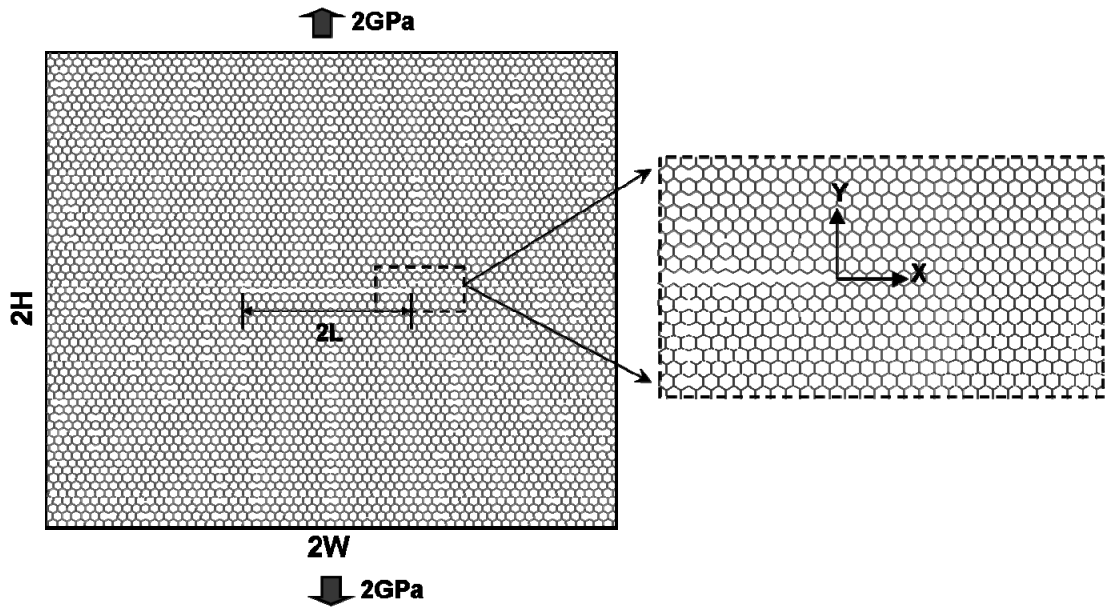
Figure 4.3.1 Atomistic structure of the graphene sheet subjected to uniaxial loading.
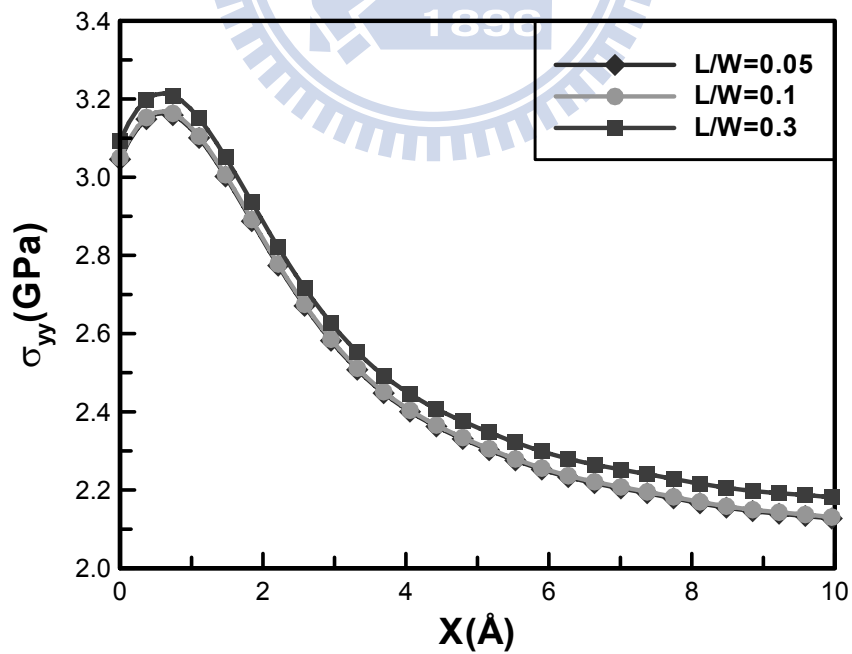
Figure 4.3.2 Local stress distribution of the graphene with crack lengths of 5 lattices and different graphene widths.
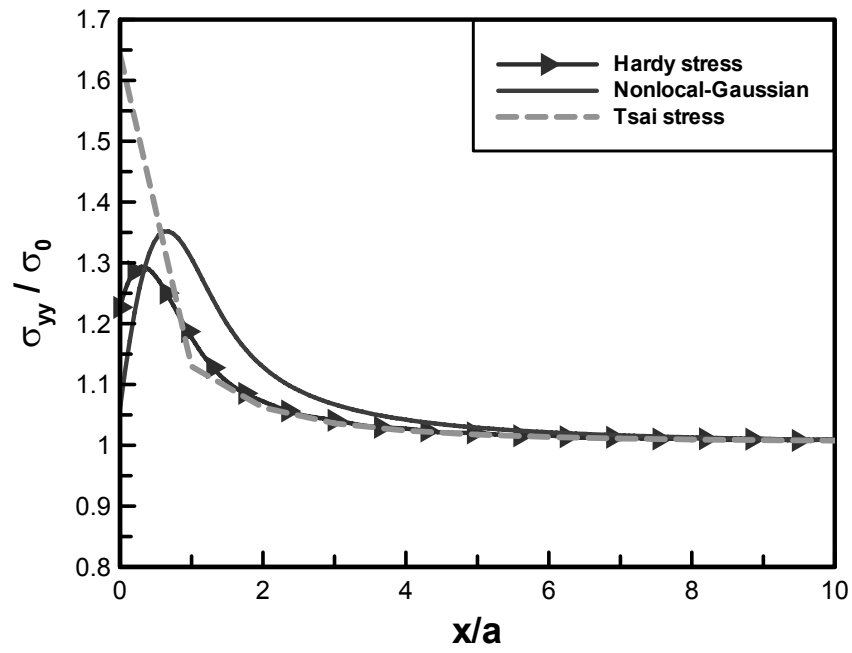
Fig. 4.3.3 Stress distribution in the graphene with crack lengths of 3 lattices
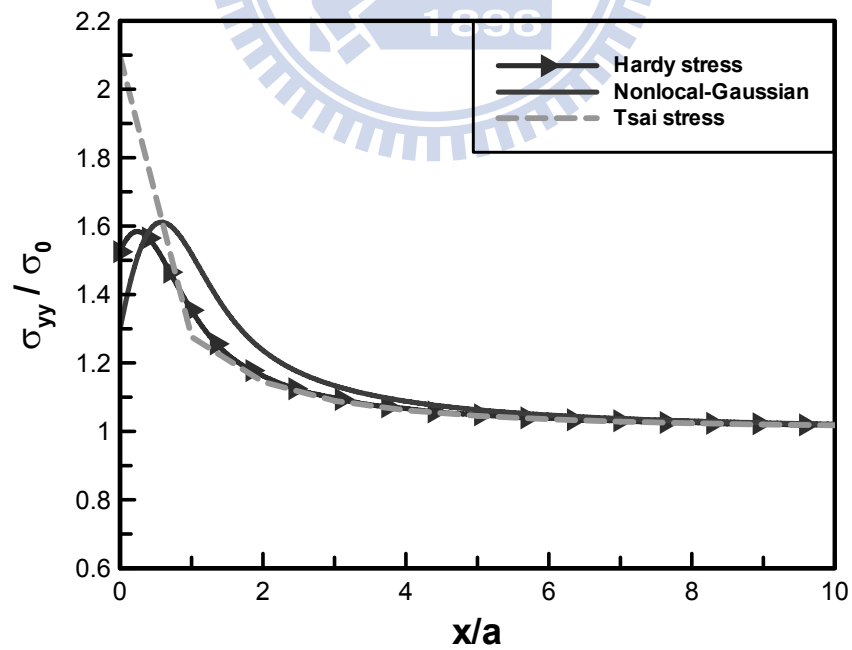
Fig. 4.3.4 Stress distribution in the graphene with crack lengths of 5 lattices
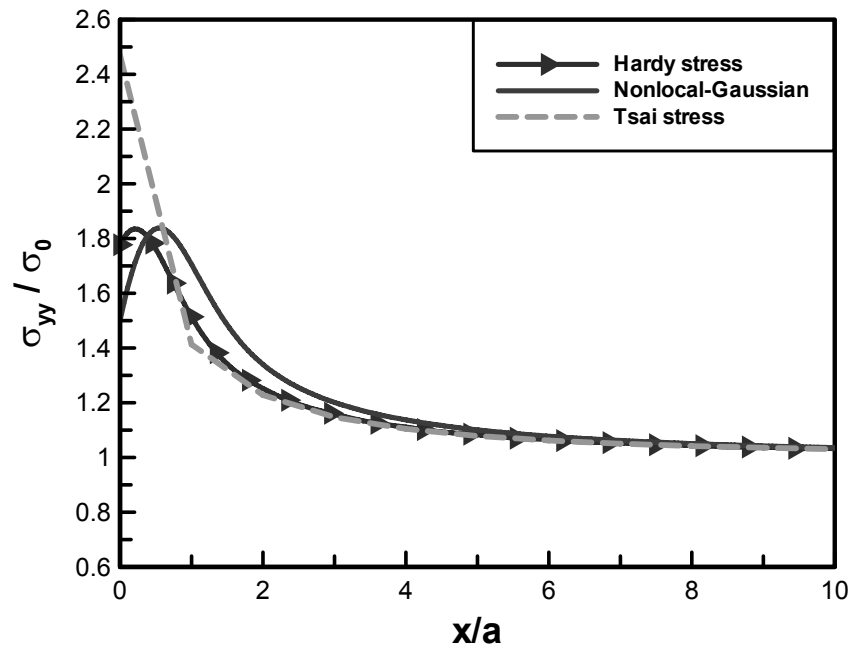
Fig. 4.3.5 Stress distribution in the graphene with crack lengths of 7 lattices

Fig. 4.3.6 Stress distribution in the graphene with crack lengths of 19 lattices

81

Fig. 4.3.7 Stress distribution in the graphene with crack lengths of 21 lattices

Fig. 4.3.8 Stress distribution in the graphene with crack lengths of 23 lattices

Fig. 4.3.9 Stress distribution in the graphene with crack lengths of 41 lattices

Fig. 4.3.10 Stress distribution in the graphene with crack lengths of 61 lattices

Fig. 4.3.11 Stress distribution in the graphene with crack lengths of 81 lattices
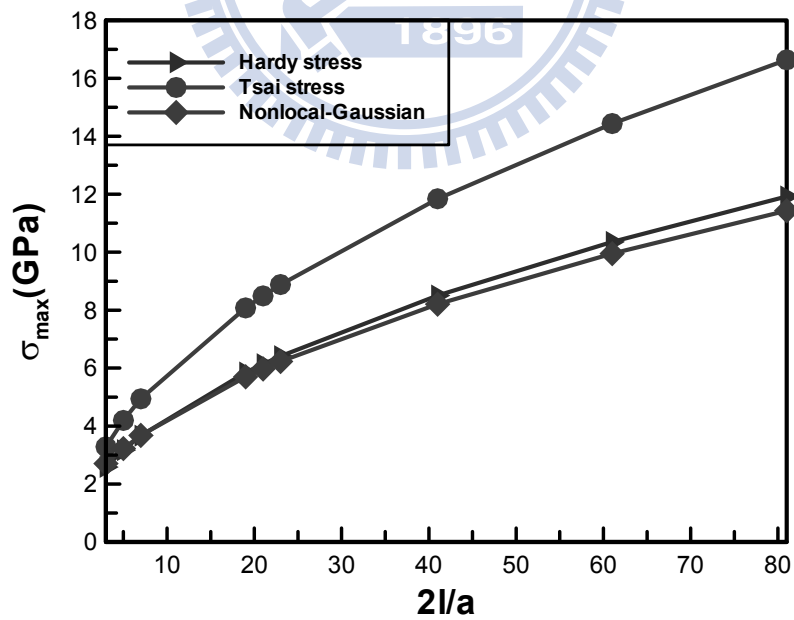
Fig. 4.3.12 Maximum local stress in the graphene with different crack lengths.
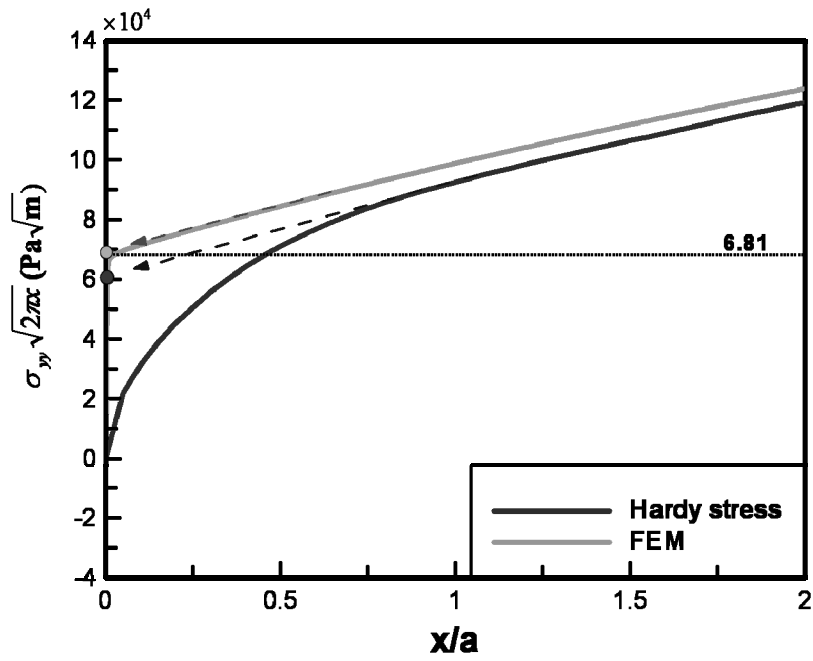
Fig. 4.4.1 $\sqrt{2\pi x}\sigma_{yy}$ plot to determine stress intensity factor of the graphene with

crack lengths of 3 lattices
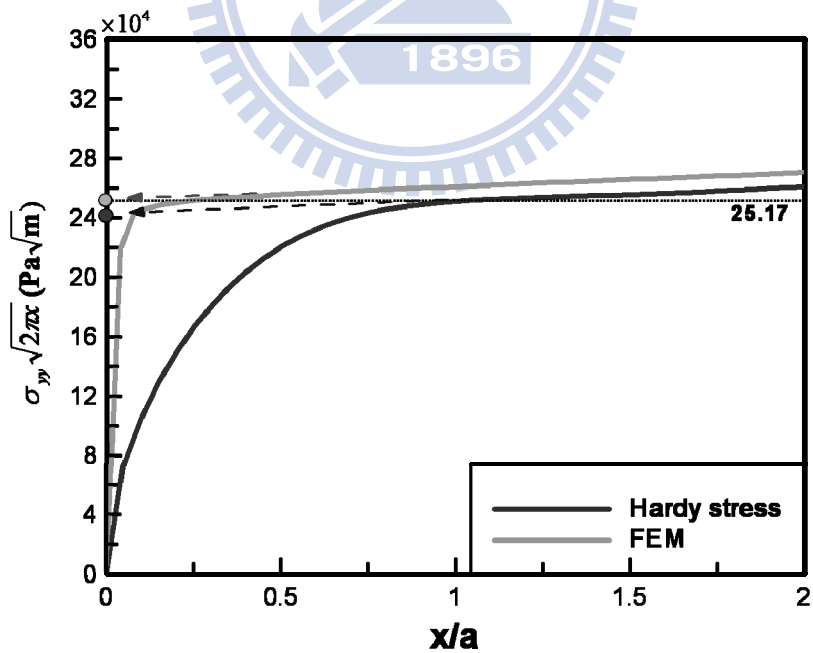
Fig. 4.4.2 $\sqrt{2\pi x}\sigma_{yy}$ plot to determine stress intensity factor of the graphene with
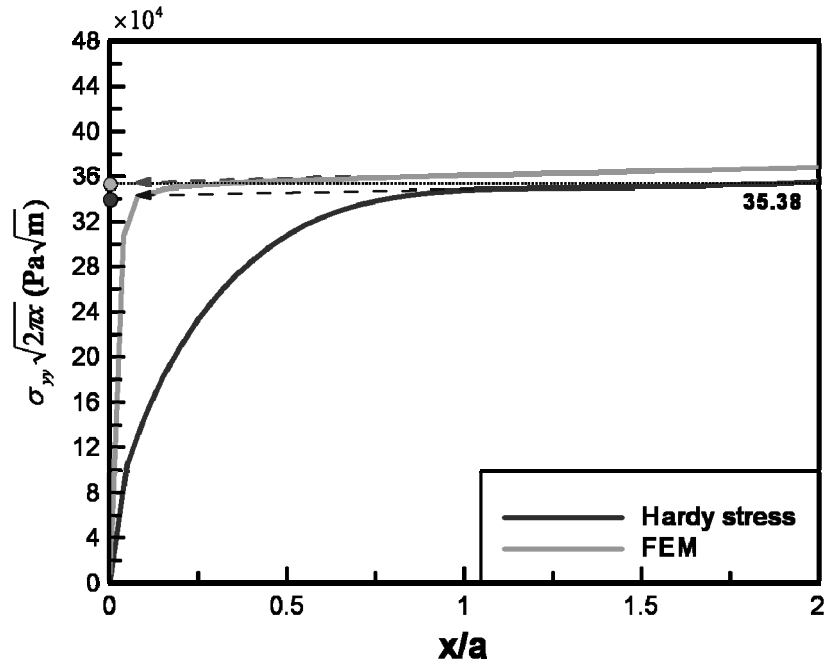
crack lengths of 41 lattices

Fig. 4.4.3 $\sqrt{2\pi x}\sigma_{yy}$ plot to determine stress intensity factor of the graphene with
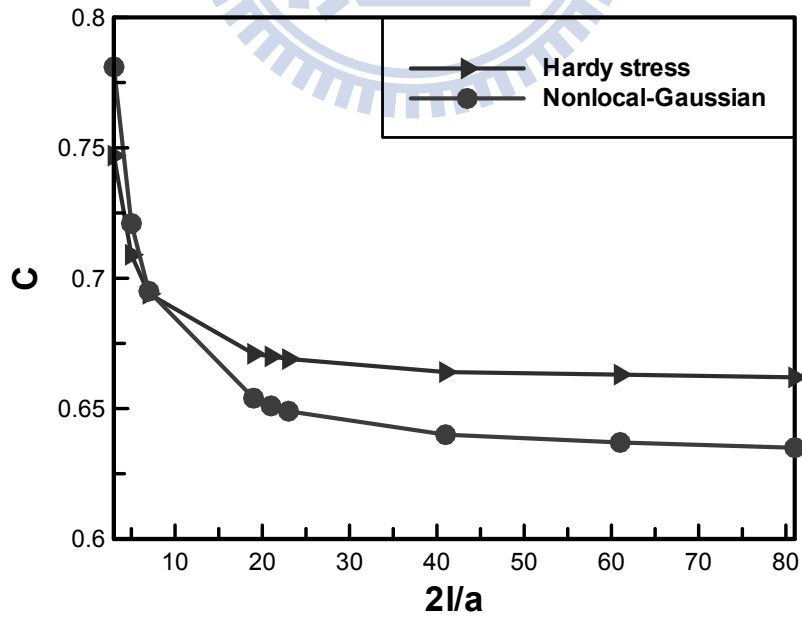
crack lengths of 81 lattices

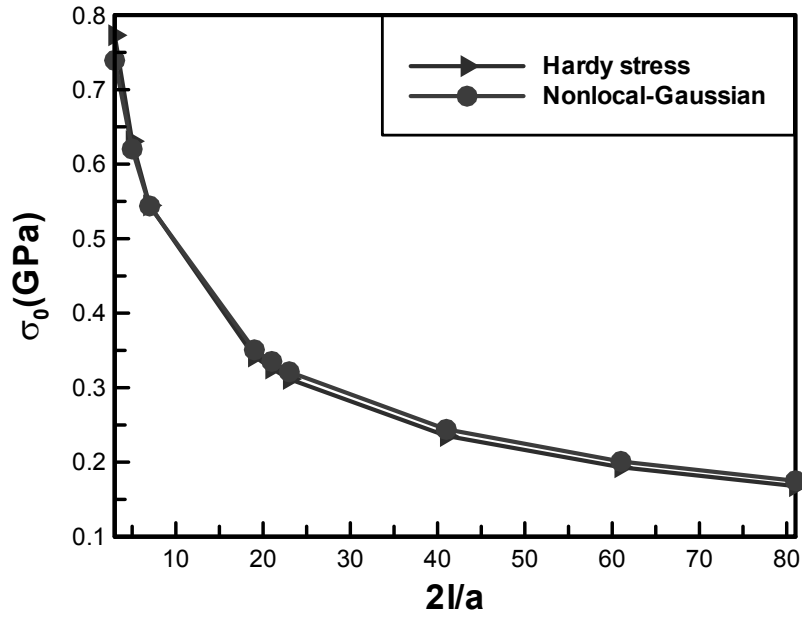Fig. 4.4.4 Stress concentration factor in discrete models with different crack lengths

Fig. 4.4.5 Applied loading to achieve σ_c with different crack lengths
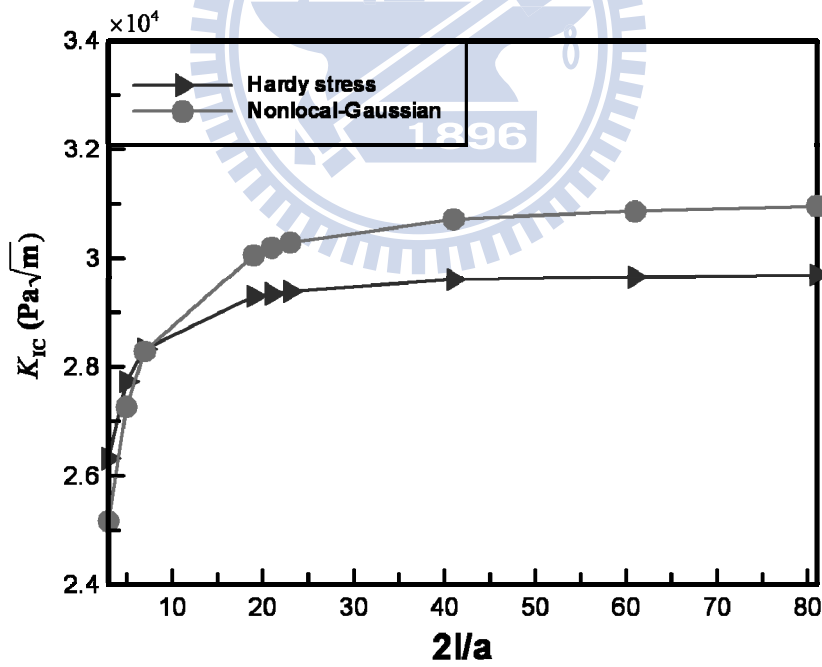

Figure 4.4.6 Fracture toughness of the graphene with different crack lengths